

2

REPORT DOCUMENTATION PAGE		FILE COPY	
1a. REPORT SECURITY CLASSIFICATION Unclassified		AD-A227 910	
2a. SECURITY CLASSIFICATION AUTHORITY		IF REPORT	
2b. DECLASSIFICATION/DOWNGRADING SCHEDULE		c release; distribution unlimited.	
4. PERFORMING ORGANIZATION REPORT NUMBER(S)		5. MONITORING ORGANIZATION REPORT NUMBER ARO 24548.3-MS-A	
6a. NAME OF PERFORMING ORGANIZATION University of Wisconsin	6b. OFFICE SYMBOL (if applicable)	7a. NAME OF MONITORING ORGANIZATION U. S. Army Research Office	
6c. ADDRESS (City, State, and ZIP Code) Department of Materials Science & Engineering 1509 University Avenue Madison, WI 53706		7b. ADDRESS (City, State, and ZIP Code) P. O. Box 12211 Research Triangle Park, NC 27709-2211	
8a. NAME OF FUNDING/SPONSORING ORGANIZATION U. S. Army Research Office	8b. OFFICE SYMBOL (if applicable)	9. PROCUREMENT INSTRUMENT IDENTIFICATION NUMBER DAAL03-86-K-0164	
8c. ADDRESS (City, State, and ZIP Code) P. O. Box 12211 Research Triangle Park, NC 27709-2211		10. SOURCE OF FUNDING NUMBERS	
		PROGRAM ELEMENT NO.	PROJECT NO.
		TASK NO.	WORK UNIT ACCESSION NO.
11. TITLE (Include Security Classification) PHASE SELECTION AND PROCESSING OF HIGH TEMPERATURE INTERMETALLIC ALLOYS			
12. PERSONAL AUTHOR(S) J. H. Perepezko			
13a. TYPE OF REPORT Final Report	13b. TIME COVERED FROM 86/10/01 TO 90/02/28	14. DATE OF REPORT (Year, Month, Day) 90/9/18	15. PAGE COUNT 106
16. SUPPLEMENTARY NOTATION The view, opinions and/or findings contained in this report are those of the author(s) and should not be construed as an official Department of the Army position, policy, or decision, unless so designated by other documentation.			
17. COSATI CODES		18. SUBJECT TERMS (Continue on reverse if necessary and identify by block number)	
FIELD	GROUP	Intermetallics, High Temperature, Solidification, Phase Equilibria, Kinetics, Thermal Stability, Powder Processing, Undercooling, Nucleation, Metastable Phases, Aluminides,	
19. ABSTRACT (Continue on reverse if necessary and identify by block number)		Niobium Alloys	
<p>A crucial issue in the development of high temperature intermetallic systems for structural applications is the formulation of materials processing strategies in order to achieve controlled microstructures that are designed to provide for the required mechanical performance in elevated temperature aggressive environments. In the research effort at the University of Wisconsin-Madison an integrated approach coupling processing with microstructure control as guided by the operative phase equilibria has been used to identify several intermetallic alloys that show promise for further development.</p> <p>The processing efforts have been directed to examining the phase selection, solidification pathways and product phase thermal stability to provide a basis for microstructural development and alloy design. In Ti and Nb base alloy systems such as Ti-Al, Ti-Al-Nb, Nb-Cr and Nb-Al the formation of alternate phases has been identified and examined in terms of the operative kinetics and metastable phase equilibria. Powder samples have been examined following atomization and containerless drop tube processing to analyze solidification structure development. Long term microstructural stability is a key issue in particulate consolidation and high temperature application. A detailed study in Ti-Al alloys has demonstrated that the thermal stability of ($\alpha_2 + \gamma$) phase structures can be change dby more than 150° C by controlled manipulations of the microstructural morphology. In order to analyze the observed microstructural variations kinetics models have been developed to describe the competitive phase reactions during powder solidification and solid state treatment.</p>			
20. DISTRIBUTION/AVAILABILITY OF ABSTRACT <input checked="" type="checkbox"/> UNCLASSIFIED/UNLIMITED <input type="checkbox"/> SAME AS RPT. <input type="checkbox"/> DTIC USERS		21. ABSTRACT SECURITY CLASSIFICATION Unclassified	
22a. NAME OF RESPONSIBLE INDIVIDUAL		22b. TELEPHONE (Include Area Code)	22c. OFFICE SYMBOL

DTIC
 ELECTED
 OCT 25 1990
 S & E

390

I.	Introduction	1
II.	Research Accomplishments in the Ti-Al Alloy System					2
III.	Alloy Design Strategies in the Ti-Al-Nb Alloy System					33
IV.	Research Accomplishments in Other Alloy Systems					39
	A. Nb-Al Alloy System	39
	B. Nb-Cr Alloy System	41
	C. Al-V Alloy System	43
V.	Summary Highlights	46
VI.	Figures	51
VII.	References	102
VIII.	Publications of the Current Program	104
IX.	Presentations	105
X.	Participating Scientific Personnel	106

Accession For	
NTIS GRA&I	<input checked="" type="checkbox"/>
DTIC TAB	<input type="checkbox"/>
Unannounced	<input type="checkbox"/>
Justification	
By _____	
Distribution/	
Availability Codes	
Dist	Avail and/or Special
A-1	

I. Introduction

The research activities in materials processing at the University of Wisconsin-Madison include several interrelated efforts which are focused in the general area of rapid solidification and powder processing. A major effort is being directed towards the production of novel microstructures in high temperature intermetallic alloys in powder form. In conjunction with the experimental studies several approaches are being examined to develop models for the analysis of microstructural evolution and to provide a basis for predictive capability.

The processing efforts are directed to examining phase selection, solidification pathways and thermal stability of solidification products to provide a basis for microstructural development and alloy design in high temperature intermetallics in titanium and niobium base alloy systems. The formation of alternate metastable phases is controlled by the operative phase selection kinetics which are being identified in Ti-Al, Nb-Cr and Ti-Al-Nb alloys. Powder samples that have been produced by atomization or processed in a containerless drop tube facility serve as useful experimental samples for the analysis of nucleation kinetics control. The experimental results on phase selection as a function of undercooling and alloy composition in Ti-Al alloys are being integrated with a heat flow analysis to develop solidification pathways for process control and microstructural analysis.

The development of an effective consolidation procedure for particulates and the long term stability of microstructures to

elevated temperature exposure are key elements in the production of advanced intermetallic components. These issues have been examined in terms of the influence of solidification processing and alloy composition in Ti-Al alloys.

The final microstructure represents the combined influence of the phase selection, the solidification pathway, the thermal stability and the diffusional interactions. The analysis of processing and microstructure development is summarized in the following sections. The experimental studies in the binary system are now complete. In addition the results from new studies on the Nb-Cr system have developed to the point where it is now possible to identify some new opportunities for microstructure control and processing that are being pursued in the continuing research effort.

II. Research Accomplishments in the Ti-Al Alloy System

For some selected alloy compositions a comparison of microstructures developed with different processing methods was made including atomization, plasma rotating electrode process (PREP), drop tube processing (DT) and melt spinning. Some work on the decomposition reaction of rapidly solidified products was pursued to begin an evaluation of the reaction kinetics.

The proper interpretation of the evolution of the solidification product structure phase selection and microstructural morphology is strongly dependent on accurate information about the phase diagram. This is important for both conventional solidification processing as well as for rapid

solidification.

In the Ti-Al system the proper representation of the phase equilibria has been an issue of debate and controversy in the literature for more than thirty years. In a recent assessment by Murray (1) an attempt was made to resolve the phase equilibria. The resulting phase diagram and thermodynamic evaluation from this assessment was used in our initial work to provide a basis for the interpretation of solidification processing. However, a phase diagram evaluation and critical assessment are only as reliable as the information that is used for the analysis.

There are several regions in the Ti-Al phase diagram where the thermochemical and phase equilibria information are incomplete or of questionable reliability. One of these regions involves the liquidus and solidus phase boundaries of the titanium rich alloys which are of vital importance in solidification analysis. The description of the liquidus and solidus boundaries has been questioned further with the observation of hexagonal dendrite morphologies in arc-cast ingots. As a result of these questions further experiments to identify the phase equilibria were performed at the University of California-Santa Barbara and at the University of Wisconsin-Madison. The results of the experimental work at Wisconsin have been included in Figure 1 and were used for the analysis of solidification reactions. Although refinements in the phase diagram may be expected as the experimental work and modeling proceed further, it now appears that the key essential details of the phase equilibria are established in the Ti-Al

system. It is also worthwhile to note that there are some important differences between the current phase diagram assessment and the version that was used in the initial interpretation of solidification structure development.

Rapidly Solidified Powders

a) Ti-25 at. % Al (Ti_3Al)

Under equilibrium conditions, an alloy of this composition would solidify as (bcc) beta-Ti, transform to (hcp) α -Ti upon cooling in the solid state and order to a (DO_{19} , Ni_3Sn -type) α_2 structure at lower temperature. To evaluate the influence of rapid solidification processing on microstructural development in Ti_3Al , powder prepared by a plasma rotating electrode process (PREP) was examined using x-ray diffraction and microscopy (optical polarized light and SEM).

X-ray analysis of the Ti_3Al powders indicated a hexagonal structure with the splitting of peaks corresponding to lattice planes with non-zero h and k values. The peaks correspond to α and α_2 phases with a shift in peak locations. The c_0 lattice parameter for both phases was identical at approximately 0.46 nm, while the a lattice parameters were about 0.58 nm for α and 0.565 nm for α_2 (2). Following an anneal for 1 hour at 600°C, the x-ray reflections were reduced to those of the equilibrium α_2 structure as shown in Figures 2 and 3, with lattice parameters: $a_0 = 0.577$ nm, and $c_0 = 0.464$ nm.

Metallographic examination of internal sections of the Ti_3Al PREP powders revealed a martensitic microstructure, with no

dendrites present (Figure 4). Prior β grain boundaries were visible in some of the particles with a ratio of particles with no grain boundaries to grain boundary containing particles of 4 to 1. The β grains were equiaxed with a grain size of about 75 μm indicative of cooling rates on the order of 500°C/sec (3).

SEM analysis of the surfaces of the powders revealed that half of the powders show partial shrinkage solidification relief on one side of the surface in a "soccer ball" cellular-dendritic pattern (Figure 5), and the remainder are generally smooth and featureless with some martensitic surface texture visible (Figure 5b). The dendrite arm spacing was measured from the powder surface as 2-3 μm . No internal dendrite morphology was apparent.

Based upon these observations, solidification in the Ti-25 at.% Al powder followed the equilibrium pathway with the formation of beta-Ti from the melt, transformation of beta-Ti in the solid state to α -Ti, and subsequent partial ordering of α -Ti to α_2 .

b) Ti-50 at. % Al (TiAl, γ -phase)

Under equilibrium conditions, an alloy of equiatomic composition solidifies through a peritectic reaction, $\alpha\text{-Ti} + \text{L} \rightleftharpoons \gamma \text{ (TiAl)}$, with TiAl having an ordered Ll_0 (fct, CuAu-type) structure. The α -phase then undergoes a solid state transformation to the γ -phase.

To evaluate the influence of rapid solidification processing on microstructural development in TiAl, powders produced through PREP were classified according to size and analyzed using x-ray

diffraction and SEM. In each powder size range two crystal structures were detected, the equilibrium TiAl phase and a metastable hexagonal structure indexed according to the ordered α_2 phase. While the superlattice reflections were clearly discernable for TiAl, those of α_2 were difficult to discern due to their inherently low intensities and their overlap with TiAl reflections for an equiatomic alloy. The relative abundance of the two phases varied with powder size, with the metastable product decreasing in amount as the powder size increased. As illustrated in Figure 6, the finest powder ($<44 \mu\text{m}$) was comprised predominantly of the α_2 phase, with only a minor fraction of the total volume ($<10\%$) represented by the equilibrium TiAl structure. The lattice parameters for α_2 were determined as: $a_0=0.5692 \text{ nm}$, $c_0=0.4602\text{nm}$. These parameters are consistent with those predicted for the equiatomic composition based upon a linear extrapolation of data for equilibrium α_2 , as illustrated in Figure 7. As the powder size increased the volume fraction of α_2 decreased, with TiAl becoming the dominant phase for powder larger than approximately $60 \mu\text{m}$, as illustrated in Figure 8.

Microstructural examination of the powder revealed the presence of both single and dual phase particles. Furthermore, within the single phase group, two basic types of particles were observed, one showing no surface relief on either external surfaces or on etched cross-sections, and the other having surface and internal features characteristic of a martensitic transformation product. Examples of both particle types are presented in Figures 9 and 10. The dual phase powder, as

illustrated in Figure 11, contained varying amounts of an initial single phase morphology (i.e. region "A" in Figure 11), usually originating at the particle surface, with the remaining volume of each particle containing a dendritic two-phase structure having approximately a constant dendrite arm spacing. The etching response of the single phase region and radiating dendrites was similar to that of the featureless single phase powder. The morphology of the dendritic structure showed a consistent tendency for the secondary arms to grow at angles near 60° with respect to the primary arms. The primary dendrite arms also reflected this growth pattern, with a six-fold rotational symmetry often evident, as seen in the micrograph of Figure 12. This type of growth morphology is indicative of a hcp structure, for which the preferred growth directions are of the $\langle 10\cdot0 \rangle$ type. Thus, for both the dual phase and single phase powder (showing no surface relief), the active solidification pathway involved the nucleation and growth of a hcp α -Ti structure from the melt. Based upon x-ray evidence, the final portion of solidification in the dual phase powder occurred with the formation of TiAl in the interdendritic regions. The increase in the relative abundance of the equilibrium product with powder size observed through x-ray analysis was reflected in powder microstructure by an increase in the volume fraction of the interdendritic TiAl. The rapid α_2 transformation kinetics allows ordering to occur upon cooling in the solid state. An alternative solidification pathway was followed for the major fraction of the remaining single phase powder (i.e. those showing surface relief)

involving nucleation and growth of beta-Ti from the melt, subsequent martensitic transformation to α -Ti in the solid state followed by ordering to α_2 . A final type of particle was observed occasionally in the larger size powder ($>70 \mu\text{m}$), in which the cross-sectional etching response appeared entirely as the TiAl phase.

As with the total volume fraction of metastable α_2 phase, the distribution of single and dual phase particles varied with powder size. A summary of the microstructural analysis, presented in Table I, indicates that single phase particles solidifying as α -Ti dominate in the finest size range ($<35 \mu\text{m}$), while the dual phase particles dominate the in the larger powder sizes. This trend is consistent with a decrease in melt undercooling with increasing powder size, prior to nucleation of the α -Ti phase. The increase in percentage single phase beta-Ti particles in the intermediate sizes illustrates the operation of competing nucleation kinetics over a given cooling rate/undercooling regime.

Containerless Drop Tube Processing Containerless drop tube processing provides a means of rapidly solidifying powders in a laboratory facility under a variety of controlled conditions. As illustrated in Figure 13 the laboratory scale (3m) drop tube used in the investigation is based on an environmentally isolated chamber with provision for sample treatment under vacuum or under a purified Ar or He gas atmosphere. Melting was carried out using a graphite heating assembly with approximately 100°C

TABLE I

PRODUCT STRUCTURE ABUNDANCE

Powder Microstructure (Solidification Path)	Distribution (Powder Diameter, μm)					
	<35	36-45	46-65	66-90	91-120	121-150
Single Phase						
(L to α -Ti)	66%	22%	10%	3%	2%	<1%
Single Phase						
(L to beta-Ti)	1%	2%	4%	11%	9%	2%
Dual Phase						
(L to α -Ti+TiAl)	32%	75%	84%	84%	86%	95%
Single Phase						
(L to TiAl)	<1%	<1%	2%	2%	3%	2%

superheat applied to the falling powder.

a) Ti-31 at. % Al

Initial experiments on a Ti_3Al alloy of composition Ti-31 at.% Al, involved heating the powders to a temperature of approximately 1450°C during free fall under a He gas environment. This temperature lies significantly above the $\alpha \rightarrow \beta$ transition temperature, but below the β solidus, which allowed the solid state transformation from β upon cooling to be examined independently of solidification. X-ray analysis showed a splitting of the hexagonal peaks, similar to the PREP Ti_3Al powder discussed previously. The "standard" in this instance was annealed Ti-31 at.% Al powder, having lattice parameters of: $a = 0.5761$ nm, $c = 0.4641$ nm. The peak splitting implies that incomplete ordering of the α to α_2 occurred during the rapid cooling from β . Microstructural examination, showed the presence of an acicular martensitic structure in all of the rapidly quenched particles.

Following the solid state treatments, powder samples were processed above the liquidus (to approximately 1750°C) in a He environment, with the spheroidization of all particles implying complete melting during free fall. As in the solid state quenched powder, x-ray analysis of the powder processed above the liquidus indicated incomplete ordering to α_2 , as may be seen by the splitting of x-ray reflections in Figure 14. As the powder size increased, the volume fraction of disordered α declined. Microstructural examination of the liquid quenched powder showed an acicular martensitic structure in all powder particles, an

example of which is presented in Figure 15, which is consistent with β formation from the melt.

b) Ti-40 at. % Al

For Ti-40 at.% Al alloys the initial sample preparation required homogenization in the single phase α -Ti field, at a temperature of 1150°C, and rapid quenching to avoid precipitation in the solid state. Beginning with this single phase α_2 powder, samples were processed under a He gas environment, with the powder heated above the liquid to approximately 1700°C.

X-ray analysis of the drop tube processed powder revealed the presence of both the ordered and disordered hexagonal phases, however, the variation in abundance of the phases with powder size was opposite to that observed in the lower Al content alloys. As illustrated in Figure 16 the finest powder (<37 μ m) contained nearly equal amounts of the order α_2 and disordered α phase, while the larger powder (37-74 μ m) was dominated by the disordered α phase.

Metallographic examination revealed the presence of two microstructural variants in the drop tube processed powder. The first consisted of a martensitic microstructure similar to that found in the Ti-31 at.% Al alloy (Figure 15). The second was a cellular morphology, showing no evidence of a solid state martensitic transformation. While the cells were often difficult to discern due to a very even etching response across each particle, virtually all of the non-martensitic particles did show some evidence of cell formation. The fraction of the powder population forming as cellular particles increased with

decreasing powder size, as summarized in Figure 17.

While the presence of martensitic powder indicated the formation of β from the melt, the occurrence of cellular, non-martensitic powder corresponded to α formation. A correlation of the α : α_2 volume fraction ratio with microstructure and powder size in the Ti-40 at.% Al and lower Al content alloys implies that the formation of β from the melt, and its subsequent transformation to α through the martensitic reaction, inhibits the $\alpha \rightarrow \alpha_2$ ordering kinetics in powder samples. Alternatively, the formation of α from the melt produces little barrier to ordering on the hexagonal lattice. Support for this hypothesis was obtained by reprocessing the Ti-40 at.% Al powder under an Ar atmosphere, having a thermal conductivity approximately one order of magnitude lower than that of He gas. X-ray analysis of the Ar processed powder showed a dominance of the disordered α phase, even in the finest size range, while microstructural examination revealed martensitic patterns in virtually all powder sizes, as indicated in Figure 17.

c) Ti-48 at. % Al

Drop tube processing of the Ti-48 at.% Al alloy powder under a He gas environment produced microstructural modifications similar to those observed in the atomized powder discussed previously. X-ray analysis, as illustrated in Figure 18, showed a dominance of the α_2 in finest powder, with a small amount (<10%) of the γ phase also detected. No evidence of peak splitting was observed, implying that the hexagonal phase was

ordered, and the lattice parameters of the α_2 were in agreement with those of the atomized powder. As the particle size increased, the volume fraction of γ increased, becoming the dominant phase for powder of size greater than approximately 100 μm .

Microstructural examination revealed the presence of cellular and single phase particles, as illustrated in Figure 19, with neither showing evidence of a martensitic transformation. Based upon microstructural observations and x-ray analysis, the solidification pathway followed with $L \rightarrow \alpha$, with γ forming near the end of solidification in the intercellular regions of the dual phase particles. Through drop tube processing, the percentage of the powder population occurring as single phase particles increased in the smaller size ranges more quickly than that of the atomized powder.

Drop tube processing of the Ti-48 at.% Al powder under an Ar gas environment reduced greatly the percentage of single phase particles, with a corresponding increase in cellular powder, however, no evidence of martensitic patterns or disordered α were detected in the microstructure. A summary plot of the microstructural observations is presented in Figure 20.

d) Ti-50 at. % Al (TiAl- γ)

Containerless drop tube processing was used to remelt and solidify the PREP powder during free fall. X-ray diffraction of <44 μm powder following drop tube processing, as presented in Figure 21, showed the major constituent as being a hcp α -phase structure, with the minor phase being TiAl.

Microstructural examination revealed both single and dual phase particles, with the single phase powder showing no evidence of a martensitic transformation. The dual phase powder, examples of which are presented in Figure 22, contained typically a single phase region around the perimeter of the droplet from which a coarsened dendritic structure developed in the powder interior. The thickness of the surrounding single phase region varied from approximately 0.5 to 3 μm between individual particles, while the phase spacing in the interior remained approximately constant. Shrinkage cavities were also frequently observed in the powder interior (Figure 22). The development of this type of morphology illustrates the dominance of surface nucleation during containerless processing. Based upon the x-ray and microstructural observations, the solidification pathway followed during drop tube processing is essentially the same as that of PREP, with α -Ti forming from the undercooled melt and TiAl forming during the final stage of solidification in the intercellular regions. The development of a coarsened dendritic morphology in the drop tube processed PREP powder sample may reflect a difference in cooling conditions during and after recalescence in the two powder processing techniques.

e) Ti-52 at. % Al

As the Al content was increased to 52 at.%, a consistent trend in microstructural evolution during drop tube processing was observed. X-ray analysis for samples processed in a He environment confirmed the presence of ordered α_2 , having lattice parameters of: $a = 0.5740 \text{ nm}$, $c = 0.4616 \text{ nm}$, and the equilibrium

γ phase having lattice parameters of: $a = 0.3983$, $c = 0.4072$ nm ($c/a = 1.022$). Once again no evidence of disordered α was observed for the He processed samples. Based upon x-ray analysis, the volume fraction of γ increased with powder size, becoming the dominant constituent for powder sizes larger than approximately $50 \mu\text{m}$. For all powder size ranges, the ratio of α_2 to γ was lower than in the equiatomic alloy powder.

Microstructural examination indicated a dominance of cellular solidification structures. These dual phase particles were similar to those of the equiatomic alloy, however, no single phase region was observed around the perimeter of the particles. Single phase α_2 particles were only observed in the finest size range ($<30 \mu\text{m}$), with the percentage of single phase powder being approximately 10%.

f) Ti-55 at. % Al

An alloy of composition Ti-55 at.% Al represents the Al rich limit of single phase TiAl. Drop tube processing of this alloy under a He gas environment showed a dramatic change in solidification behavior compared to the lower Al content alloys.

X-ray analysis, indicated the dominance of γ in all sizes ranges, with only the finest powder containing significant amounts ($\sim 10\%$) of metastable α_2 . Microstructural examination revealed cellular morphologies in all powder size ranges, as illustrated in Figure 23, with a second phase having a plate-like morphology observed often at the cell boundaries. Based upon the x-ray and microstructural evidence, the solidification pathway followed for the Ti-55 at.% Al powder involved predominantly the

formation of γ from the melt, with the final intercellular liquid freezing as a second intermetallic compound, in agreement with the equilibrium phase diagram. Based upon x-ray evidence, initial solidification in a portion of the finest powder ($<37 \mu\text{m}$) may have involved α formation from the melt, however, little microstructural evidence was found to support this hypothesis, as might be expected from the limited volume fraction present in the powder. For powder processed under an Ar atmosphere, γ was the only phase detected in all powder size ranges.

Summary of Drop Tube Processing and Solidification Behavior

One of the most significant advantages in using drop tube processing of powders was the ability to control processing conditions for a variety of alloy compositions. With this approach, the influence of individual processing parameters and powder characteristics could be evaluated in terms of microstructural development during rapid solidification.

In summarizing the variations in solidification behavior during drop tube processing for the range of parameters considered, the two most significant variables were found to be alloy composition and powder size. As such, the variation in solidification microstructure with Al content was considered separately for "fine" ($<40 \mu\text{m}$) and "coarse" ($>40 \mu\text{m}$) powder. As illustrated in Figure 26 for "fine" powder (using powder of size $30 \mu\text{m}$ for comparison), increasing the Al content above 30 at.% encouraged the formation of α over β from the melt. The appearance of single phase α occurred for Al contents greater

than 40 at.%, reaching a maximum at approximately 50 at.%. The formation of α was terminated abruptly at Al contents greater than 55 at.% by the formation of a cellular γ structure.

A similar summary of the variation in microstructural abundance with Al content is presented in Figure 27 for "coarse" powder (taken as approximately $50\mu\text{m}$ for comparison). The general trends were similar to the "fine" powder, however the replacement of β by α formation from the melt was delayed to higher Al contents (>35 at.% Al). In addition, the formation of single phase α was suppressed, however, the maximum percentage of these particles remained at approximately 48-50 at.% Al. It should be noted that the microstructural summaries presented in Figures 26 and 27 indicate the solidification product only, and that modifications of the microstructure (e.g. ordering of α to α_2) occur in most instances upon rapid cooling in the solid state.

The influence of powder size on microstructural development can be inferred from a comparison of Figures 26 and 27. In general, decreasing the powder size encouraged the replacement of β with α formation from the melt and increased the fraction of the population occurring as single phase (α_2) particles. The influence of gas environment was similar to powder size, in that changing from Ar to He (with an increase in cooling rate) produced an effect similar to a decrease in powder size.

As a basis for the analysis of the solidification reactions it is useful to summarize briefly the broad trends observed in the binary Ti-Al alloys following rapid solidification. Table II provides a summary of the solidification pathways followed for

Table II

SUMMARY OF Ti-Al BINARY MICROSTRUCTURAL DEVELOPMENT

<u>Al Content (atomic %)</u>	<u>Processing Technique</u>	<u>Microstructural Pathway</u>
25	○ PREP	$L \rightarrow \beta (\rightarrow \alpha' + \alpha_2)$
31	■ DT	$L \rightarrow \beta (\rightarrow \alpha' + \alpha_2)$
40	■ DT	$L \rightarrow \beta (\rightarrow \alpha' + \alpha_2)$ (coarse powder in Ar) $L \rightarrow \alpha (\rightarrow \alpha_2)$ (fine powder in He)
48	▲ atomized ■ DT	$L \rightarrow \alpha + \gamma (\rightarrow \alpha_2 + \gamma)$ $L \rightarrow \alpha + \gamma (\rightarrow \alpha_2 + \gamma)$
50	○ PREP ■ DT	$L \rightarrow \alpha + \gamma (\rightarrow \alpha_2 + \gamma)$ $L \rightarrow \alpha + \gamma (\rightarrow \alpha_2 + \gamma)$
52	○ PREP ◆ MS	$L \rightarrow \alpha + \gamma (\rightarrow \alpha_2 + \gamma)$ $L \rightarrow \alpha + \gamma (\rightarrow \alpha_2 + \gamma)$
55	■ DT ◆ MS	$L \rightarrow \alpha + \gamma (\rightarrow \alpha_2 + \gamma)$ (fine powder in He) $L \rightarrow \gamma$ (coarse powder in Ar) $L \rightarrow \alpha + \gamma (\rightarrow \alpha_2 + \gamma)$

Abbreviations:

○ PREP	plasma rotating electrode processed
■ DT	drop tube processed
◆ MS	melt spinning processed
▲ atomized	atomization process

the range of alloy compositions and processing conditions evaluated in the current investigation. For the equilibrium α_2 alloys, solidification occurred through the formation of β from the melt followed by a martensitic transformation to α' and partial ordering to α_2 . As the Al content was increased to 40 at.% the finest powder processed under He gas solidified as α (followed by ordering to α_2) while the remainder formed as β from the melt. From 48 to 52 at.% Al virtually all powder and ribbon samples solidified initially as α , with γ forming near the end of solidification. In each of these alloys, as the powder size increased, the volume fraction of γ forming in the interdendritic regions increased. At 55 at.% Al, the finest powder processed under He formed a small amount of α , while all remaining samples solidified as γ from the melt. For melt spun ribbon, the solidification path remained as α , followed by γ formation in the intercellular regions.

Melt Spun Ribbon

In an alternative rapid solidification processing approach, ribbons of Ti-52 and 56 at.% Al were prepared through melt spinning onto a copper wheel in a He gas environment. Microstructural analysis was carried out using TEM.

The solidification microstructure after melt spinning was similar for both alloys, an example of which is presented in Figure 24. The dark regions tend to be convex, suggesting that they form first from the melt and share a common crystallographic orientation. Using convergent beam electron diffraction (CBED),

this dark phase was identified as having a $D0_{19}$ (α_2) structure. The phase shown in light contrast in Figure 24 was identified by CBED as having the $L1_0$ (TiAl) structure. The $D0_{19}$ phase contains a fine distribution of antiphase domains, shown in the dark field image of Figure 25 using a superlattice reflection, which suggests that the ordered $D0_{19}$ structure formed in the solid state from a disordered hcp phase. These observations suggest that the solidification pathway followed during melt spinning is the same as that of the (dual phase) powder, with the nucleation and growth of hcp α -Ti from the melt followed by the formation of intercellular TiAl and ordering of the α -Ti to α_2 in the solid state.

Discussion of Ti-Al System

Rapid solidification processing offers a greatly enhanced potential to modify microstructural development in alloys by providing alternate (i.e. nonequilibrium) pathways for solidification and subsequent solid state transformations. In evaluating potential solidification pathways and phase selection, metastable phase diagrams combined with relevant T_0 curves provide valuable guidance. For the Ti-Al alloy system, T_0 curves can be calculated using thermodynamic data from the models for the bcc and hcp crystal structures (4), as illustrated in Figure 28.

The microstructures observed in both powder processing and melt spinning imply that the hcp α -Ti phase is generally favored over competing solids. The rapid increase in the fraction of

single phase particles and in the volume fraction of metastable (hcp) product in the dual phase particles, with decreasing powder size, is indicative of an increase in undercooling with decreasing droplet size. The increased occurrence of a bcc structure over a limited intermediate size range in the PREP powder may represent the operation of a specific heterogeneous catalyst only within a well defined cooling rate/undercooling regime. The finest powder, for which the (single phase) hcp structure dominates, would then correspond to particles being free of this catalyst or experiencing cooling rates which are high enough to preclude its operation.

Influence of Alloy Composition

An effective approach for evaluating the influence of alloy composition on microstructural development in Ti-Al alloys is through a consideration of drop tube processed powder microstructures, in that all samples were exposed to a well defined processing procedure which was repeatable for a range of compositions. In the equilibrium α alloys examined (25 and 31 at.% Al), the formation of a martensitic α' product structure implies that the equilibrium solidification pathway, $L \rightarrow \beta$ ($\rightarrow \alpha'$ $\rightarrow \alpha_2$), was followed, however, little detailed information may be extracted from the microstructure regarding the level of melt undercooling experienced by the powder prior to solidification. The retention of a disordered hexagonal product structure to ambient temperature is a rare observation in Ti_3Al alloys and is worth noting. The details of the distribution of ordered α_2 and

disordered α' in the powder sample requires a detailed TEM examination, to determine if individual particles contain a mixture of the two phases, or if ordered and disordered particles exist separately throughout the population.

The observation of a hexagonal (α) product structure in powder of higher Al content (40 at.% Al) indicates the operation of an alternate (metastable) solidification pathway involving α formation from the melt (followed by ordering to α_2). The operation of this metastable pathway necessitates a certain minimum level of liquid undercooling, dictated by thermodynamics, for nucleation of the hcp phase. In order to estimate this minimum level of undercooling, the L/α and L/β T_0 curves which are shown in Figure 28 as a function of alloy composition may be used. The minimum liquid undercooling required for partitionless α solidification decreases with increasing Al content, to less than 50°C for a Ti-40 at.% Al alloy. This level of undercooling is well within the range commonly observed for RSP conditions.

For Al contents between about 45 to 52 at.% Al both the phase diagram and the T_0 curve analysis indicate a close balance of phase stability between the bcc and hcp structures. Over part of this composition range the hcp phase is stable at high temperature and its formation from the liquid represents an equilibrium solidification path. It should be noted that based on the previous phase diagram version, hcp formation in this composition range was treated as a metastable phase selection process. At low temperature the hcp phase becomes metastable and will decompose to γ or $\gamma+\alpha_2$ as established in the thermal

stability investigation. For alloy compositions between about 53 to 68 at.% Al the γ phase is the equilibrium solidification product so that any α formation in this range again represents a metastable reaction.

While the multiple phase selection options that are possible in near equiatomic alloys represent important opportunities, they also pose a challenge for kinetics analysis. Work on the analysis of solidification kinetics is in progress and is being coordinated with the thermodynamic modeling studies for near equiatomic composition alloys.

The main points of the kinetics analysis may be illustrated by a consideration of the Ti-40 at.% Al alloy where the distinction in relative phase stability is clearer. A key parameter governing the nucleation kinetics operating in an undercooled melt is the activation free energy for solid formation, ΔG^* , given by

$$\Delta G^* = A \sigma^3 f(\theta) / \Delta G_v^2 \quad (1)$$

where A is a geometric nucleus shape factor, σ is the solid/liquid interfacial energy, $f(\theta)$ represents the relative catalytic potency of a nucleation site and ΔG_v is the driving free energy for nucleation. The ΔG_v term is evaluated on a volume basis by: $\Delta H \Delta T / T_m$, where ΔH is the heat of fusion, ΔT is the undercooling and T_m is the absolute melting temperature. Considering the ΔH term, the molar enthalpy of fusion for pure Ti is larger for α than β , with the difference becoming greater with

increasing Al content. The higher density of α magnifies the molar enthalpy of fusion difference, when ΔH is converted to a volume basis. This larger heat of fusion partially offsets the undercooling advantage of β and results in the attainment of a higher driving force of α formation in a sufficiently undercooled melt. For a Ti-40 at.% Al alloy at undercoolings greater than approximately 150°C ($0.10T_1$), the driving force for α formation will exceed that of the equilibrium β phase.

In addition to the driving force for nucleation, σ and $f(\theta)$ may influence significantly the nucleation kinetics. While experimental measurements of σ are largely unavailable, some structural models of the solid/liquid interface have predicted lower values for the bcc phase than for competing close packed structures. During heterogeneous nucleation, however, the potency of the operating catalyst may alter differences in σ values, which will be reflected in the magnitude of $f(\theta)$ in equation (1). It is the combined effects of the driving force, surface energy and operating catalytic site which control phase selection in an undercooled melt, with the phase having the minimum barrier (ΔG^*) being favored.

Sample and Solidification Processing

In addition to alloy composition, other factors associated with the sample characteristics and processing conditions influence the solidification pathway followed during RSP of Ti-Al alloys. This becomes apparent when considering the variation in microstructures observed at fixed alloy compositions. For the

Ti-40 at% Al alloy, the change in phase selection from a β solidification product in coarse powder to α formation from the melt in fine powder is consistent with an increase in undercooling with decreasing powder size. The principal factors which are responsible for such an increase in undercooling are the progressive isolation of internal heterogeneous nucleation sites and increased cooling rates which accompany a reduction in powder size.

Information regarding the phase selection kinetics operating in the drop tube processed Ti-40 at.% Al alloy may be obtained from a comparison of the curves describing the variation in product structure with powder size, for samples processed under Ar and He gas environments (Figure 17). Using a heat flow model in which both radiation and convective cooling of the falling particles is considered, an expression for the cooling rate of a falling particle as a function of powder size and gas environment is given by:

$$dT/dt = -K_0(T^4 - T_0^4) - H_0(T - T_0) \quad (2)$$

where T is taken as the liquidus temperature and T_0 is the ambient temperature. The first term in equation (2) represents the contribution of radiation while the second represents the contribution of convective cooling to the overall cooling rate. The K_0 term is given by: $(\epsilon\sigma A/mc)$, where ϵ is the emissivity of the particle, σ is the Stefan-Boltzmann constant, A is the surface area, m is the particle mass and c is the specific heat.

The H_0 term is given by: (hA/mc) , where h is the heat transfer coefficient. Estimates of the specific heat and emissivity were made from weighted averages of the pure element values, while the mass was calculated from density values based upon lattice parameter measurements. Estimates of the heat transfer coefficients were obtained for a given particle size and gas atmosphere (Ar or He) using data of Clyne (5). While the values of h must be considered only approximations, they are useful for comparative purposes. Assuming Newtonian cooling conditions during free fall, the observed shift in microstructure abundance curves with change in gas atmosphere may be described by a single translation in cooling rate. In other words, the difference in powder size required to produce an equivalent volume fraction of metastable product under an Ar and He atmosphere, is approximately equal to that which would be required to produce equivalent cooling rates during free fall. For example, comparing the cooling rates of powder yielding 10% metastable product, the calculated cooling rate of the $10\mu\text{m}$ particle required in an Ar atmosphere is approximately equal to that of the $45\mu\text{m}$ particle required in a He atmosphere (8×10^5 K/sec versus 1×10^6 K/s respectively). An alternative means of expressing the equivalence in thermal conditions for drop tube processed samples is through a simple comparison of the powder diameters required to produce a given percentage of the population solidifying as α under Ar and He environments. A summary plot of this diameter comparison is presented in Figure 29, which shows that the ratio of the diameters for Ar and He processed powder remains

approximately constant for an increasing percentage of metastable solidification product. The shift in microstructure abundance curves by a simple translation in cooling rate implies the operation of a single nucleation kinetics for formation of the metastable α phase in the Ti-40 at.% Al alloy, under both He and Ar drop tube processing conditions. This direction of process control analysis is being examined further in continuing studies.

Thermal Stability

Following the solidification of intermetallic alloys in powder or particulate form subsequent processing will involve the consolidation and other possible thermomechanical treatment. From this perspective it is valuable to determine the kinetic stability of the as-solidified microstructure to elevated temperature exposure.

Differential thermal analysis (DTA) of the Ti-25 at.% Al PREP powder revealed an exothermic reaction starting at 486°C and peaking at 686°C (corresponding to decomposition) during heating. Following this treatment, as well as isothermal holding treatments at 600°C for 1 hour, x-ray analysis revealed an ordered α_2 structure, with no evidence of the disordered α phase produced during initial solidification. These observations are consistent with the nucleation and growth of ordered domains to complete the ordering transformation in the powder samples.

Analysis of the atomized Ti-48 at.% Al powder showed a similar decomposition behavior to the equiatomic PREP powder. Further information was provided through thermal cycling

treatments using DTA in which the sample was heated to various temperatures within the decomposition range, cooled, and then reheated to detect further decomposition exotherms. Using this approach with fine ($<37\mu\text{m}$) powder, the major decomposition exotherm observed during continuous heating, was found to be a series of overlapping exotherms indicating multiple decomposition kinetics.

The dominance of the metastable α_2 phase in the large, as well as fine, powder sizes allowed consideration of powder size effects on decomposition behavior. DTA of fine ($<37\mu\text{m}$) and coarse ($74\text{-}105\mu\text{m}$) powder, as illustrated in Figure 30, revealed two major decomposition exotherms, centered at approximately 640° and 725°C . While the decomposition ranges were similar for both samples, a greater percentage of the coarse powder decomposed at the higher temperature exotherm. Microstructural examination of the decomposed powder at various temperatures indicated a plate-like transformation to γ similar to the PREP powder. Complete transformation required extended annealing periods, with a typical transformed microstructure presented in Figure 31.

Analysis of the higher Al content alloys following drop tube processing showed a significant change in decomposition behavior compared to the PREP and atomized powder, as illustrated in the DTA results of Figure 32 for the Ti-48 at.% Al alloy. Virtually the entire powder sample decomposed above 675°C following drop tube processing, with the maximum occurring at approximately 725°C , and a fraction of the population decomposing at temperatures up to 800°C . Similar results were observed for the

50 and 52 at.% Al powder.

To assess the thermal stability of the metastable α_2 structure, Ti-50 at.% Al powder of size $<44 \mu\text{m}$ was processed using DTA to a temperature of 900°C . The resulting thermal trace is presented in Figure 33 which shows the major exotherm associated with decomposition occurring over a range from 600°C to 700°C , with the maximum being at approximately 640°C . Following thermal analysis, similar powder was subjected to a controlled heating cycle during x-ray diffraction under a helium atmosphere, with scans being recorded during isothermal holds at 100°C intervals. Figure 34 presents a summary of the resulting x-ray patterns. Significant decomposition of the α_2 phase begins at temperatures above 500°C , with the transformation being completed at approximately 700°C . The microstructural changes associated with decomposition are illustrated in Figure 35 for a sample held 1 hour at 600°C . Transformation of metastable α_2 occurs by the growth of TiAl plates from the coarsened interdendritic regions.

The decomposition mechanism in melt spun ribbon is similar to that of the powder samples. This can be seen in the TEM micrograph of Figure 36 which shows the development of a series of alternating parallel plates of α_2 and γ -TiAl. With continued annealing the γ plates thicken at the expense of α_2 until the reaction is complete, however the kinetics are quite sluggish due to the low mobility of the $\alpha_2 / \text{L1}_0$ interface. The low mobility may be attributed to a low energy orientation relationship between α_2 and γ , determined through TEM analysis to be:

$$\begin{aligned} (0001)_{D0_{19}} & \parallel (111)_{L1_0} \\ [2\bar{1}\bar{1}0]_{D0_{19}} & \parallel \langle 110 \rangle_{L1_0} \end{aligned}$$

Thus, the decomposition of α_2 to γ represents the ordered phase counterpart to the allotropic transformation in Co (6).

The Ti-55 at.% Al alloy powder exhibited no well defined decomposition exotherm with DTA, in agreement with the dominance of equilibrium γ product in the drop tube processed powder.

The decomposition reactions observed in the binary Ti-Al alloys can be divided into two general types: metastable $\alpha' \rightarrow \alpha_2$ (i.e. the ordering of the hexagonal lattice) and metastable $\alpha_2 \rightarrow \gamma$. The first type describes the decomposition of the Ti_3Al -base powder, while the second is characteristic of the $TiAl$ -base powder and ribbon samples. While a detailed characterization of the ordering reaction in the Ti_3Al powder would require extensive TEM examination, certain statements can be made at present. The transformation to α_2 upon heating is consistent with the nucleation and growth of ordered domains (or simply growth of fine preexisting ordered nuclei formed during initial cooling) into the disordered α' , similar to that observed previously in splat quenched Ti_3Al alloys (7). In addition, based upon isothermal heat treatment results, the ordering kinetics observed in the PREP Ti_3Al powder (as well as the drop tube processed powder) is similar to that for the splat quenched foils.

The primary focus of the decomposition analysis was on the $TiAl$ -base alloys, with the observed plate-like γ transformation

product being similar to that observed previously for decomposition of equilibrium $\alpha_2 + \gamma$ alloys (8). This transformation sequence is similar to that observed in Cu-Si alloys, for which hcp plates form in a fcc (α -Cu) matrix (9). However, in Ti-Al alloys the requirement of solute diffusion for partitioning is not extensive due to the relatively narrow $\alpha_2 + \gamma$ two phase field. The rate of decomposition of α_2 is thus dependent primarily upon the rate at which new plates of γ can nucleate in the matrix.

The observation of γ plates originating at cell boundaries in both the RSP powder and ribbon samples is consistent with previous observations and implies that sites associated with the cell/dendrite boundaries are preferred for γ formation. This may be attributed to the preexistence of γ at the boundaries and/or to a nucleation preference at the higher energy interface, both of which are consistent with the delayed decomposition of single phase α_2 particles to higher temperatures. The detection of overlapping decomposition exotherms in the near-equiatomic powder with DTA implies that the sites which initiate the transformation become active over a range of temperature. Furthermore, the change in decomposition temperature with a change in solidification morphology through drop tube processing, from fine dendrites to coarse cells, implies that the interphase area is an important factor in controlling the decomposition kinetics.

The relationship between interphase area and decomposition temperature may be considered quantitatively through a comparison of the DTA exotherms (Figure 30) and solidification

microstructures of the atomized and drop tube processed Ti-48 at.% Al powder. For both processing techniques, the constituent phases were of the same crystal structure and present in approximately equal volume fractions, with the principal difference being the scale of the cellular/dendritic microstructure. Using an image analysis technique the mean thickness of the cells/dendrites was found to be $1.3\mu\text{m}$ and $3.7\mu\text{m}$ for the atomized and drop tube processed (He) powder respectively. In analyzing the DTA results, the deviation from the baseline during heating is proportional to the rate at which decomposition occurs. The decomposition rate (r) may be represented by: $r = C \exp(-Q/RT)$, where C is a constant that is proportional to the interphase area, Q represents the activation energy for the decomposition reaction, R is the gas constant and T is the temperature. Taking the maximum in the curves (representing approximately equivalent rates of heat evolution) to imply a similar rate of decomposition of the samples, the corresponding temperatures at the maximum are: $T_{\text{at}} = 920\text{K}$; $T_{\text{dt}} = 1000\text{K}$, where "at" corresponds to the atomized powder and "dt" represents the drop tube processed powder. The ratio of the decomposition rate of the atomized powder at T_{at} to that of the drop tube powder at T_{dt} can then be expressed in terms of interphase area (A) as: $(A_{\text{at}}/A_{\text{dt}}) = \exp [(-Q/R) (\Delta T/T_{\text{at}}T_{\text{dt}})]$ where ΔT is equal to $(T_{\text{at}} - T_{\text{dt}})$, or -80K . In order to evaluate the ratio of interphase areas, an assumption must be made that the volume of a powder particle is equal to the sum of the average surface area of cells/dendrites in that particle.

Assuming the geometry of the cells/dendrites to be right circular cylinders, the ratio of the total interphase areas then reduces to:

$$(A_{at}/A_{dt}) = [\rho_{at}(\rho_{dt})]^2/\rho_{dt}(\rho_{at})^2]$$

where ρ is the cell/dendrite diameter. Using the measured values for the feature size, the ratio of total interphase area is calculated to be 2.9. Substituting this value into the rate equation, along with the appropriate temperatures, provides an estimate for the activation energy of the decomposition process of 1×10^5 J/mole. This activation energy is similar to those estimated for the growth of ordered α_2 domains, for which values of 1.1×10^5 , 2.68×10^5 and 1.77×10^5 J/mole have been reported (10-12). This approximate agreement supports the assumption of a relationship between interphase area and decomposition temperature, implying that the decomposition rate is increased as the interphase area (i.e. sites for decomposition) increase. This analysis accounts for the change in decomposition behavior with increasing powder size for the atomized Ti-48 at.% Al powder (and similar results for the equiatomic alloy), for which an increase in decomposition temperature was observed with increased powder size and corresponding dendrite spacing.

III. Alloy Design Strategies in the Ti-Al-Nb Alloy System

Some of the most attractive aluminides from the viewpoint of low density and high temperature potential are those in the Ti-Al system: α_2 -Ti₃Al (DO₁₉), γ -TiAl (L1₀), η -TiAl₃ (DO₂₂) and also in the Nb-Al system: δ -Nb₃Al (A-15) and η -NbAl₃ (DO₂₂). In fact a

few alloy compositions based upon Ti_3Al with Nb additions have been developed and are being examined in high temperature applications (13). There have also been several studies (14-17) of some of the phase relationships in α_2 alloys with Nb additions which have revealed that at least two ternary phases, a B2 phase with a CsCl structure and an θ phase with an orthorhombic structure are present in this system. Other studies (18) on several ternary alloys have indicated that the B2 phase field may be quite extensive at high temperature and yield alloys which exhibit a variety of decomposition products upon cooling including $B8_2$ and ω structures. The reported investigations on the influence of Nb additions on the phase relations in γ -TiAl alloys have also been quite limited. However, it has been established that in γ -TiAl and in α_2 - Ti_3Al , Nb substitutes preferentially on the Ti sites (19). In the B2 phase Nb substitutes preferentially on the Al sites (20). In some of the current studies a systematic examination of the ternary equilibria has been undertaken which involves the mapping of the liquidus surface, the determination of an isothermal section at 1200°C and the investigation of selected isoplethal sections.

The isothermal section for the Ti-Al-Nb system is shown in figure 37 for 1200°C. There are several features of importance for high temperature alloy design and processing. For example, the $Al_3(TiNb)$ intermetallic phase with a DO_{22} structure often appear as essentially stoichiometry line compounds in binary alloys. However, ternary solutions between two isomorphous phases such as Al_3Ti and Al_3Nb can show a range of existence off

the stoichiometric value. A single phase region with a range of composition is attractive in terms of the ease of processing compared to a line compound. Similarly, the ternary solutions of several of the binary phases such δ , σ , γ , α and β have been determined to be extensive.

At high temperature the phase equilibria for Ti rich alloys is clearly dominated by bcc phases. Since the solubility range of the β phase is likely to be sensitive to temperature, this variation has been analyzed to aid in the design of multiphase alloys. The high temperature bcc structure has been observed to undergo decomposition into a number of other structures depending on the composition and cooling rate.

A feature of special importance is the isolated single phase B2 region indicated in figure 37. Evidence for the existence of an ordered bcc phase (B2) was found in alloy 36. The microstructure of alloy 36 given in figure 38 is composed of clear grains and grains containing a high density of fine precipitates. The clear grains were identified by selected area of diffraction (SAD) as the α_2 phase. The precipitate bearing grains were identified by SAD and by convergent beam electron diffraction (CBED) as having the B2 structure, while the precipitates were identified by SAD as having the B8₂ structure. The B8₂ phase is one of the several decomposition products of the B2 phase. The presence of precipitates in the B2 phase indicates that some transformation occurred during cooling of the alloy. Therefore, it is possible that the B2 phase may also be a decomposition product of a disordered bcc phase that existed at

1200°C.

The high temperature form of T₂ at 1200°C also appears to be a bcc type structure. The initial boundary of the T₂ phase was defined by tie lines, based on EPMA, of alloys 15, 33 and 50. Examination of alloy 50 reveals large γ grains, occasionally separated by narrow regions composed of alternating α_2 and γ laths. These laths have a distinct orientation relationship. This structure is common in binary alloys with a composition in the two-phase region between γ and α_2 . The microstructure of alloy 15 shown in figure 39 is composed of two phases. One phase in alloy 15 appears smooth and clear. Based upon SAD and CBED, this is the α_2 phase. Figure 39 shows that the second phase, corresponding to T₂ has decomposed during cooling. The decomposition structure, figure 39b is made up of alternating lamellae. The clear lamellae are identified as α_2 while the spotted lamellae are identified as the B2 parent and B8₂ precipitate structure.

The evidence from alloy 15 indicates that the T₂ phase present at 1200°C undergoes transformation during both rapid and slow cooling. To address this problem, alloy 101 in the center of the T₂ phase field was examined and the microstructure is shown in figure 40. Alloy 101 is composed primarily of large grains filled with unidirectional laths. These laths represent an alternating α_2 and γ structure also found in alloy 50 and confirmed by TEM analysis.

In order to determine whether the α_2/γ lath structure reflects very slow kinetics for equilibration during annealing or

rapid decomposition during cooling, alloy 101 was subjected to an annealing and quenching treatment. The optical microstructure of this quenched material is shown in figure 40b. The major difference between the slow cooled and quenched microstructure is the presence of a few clear blocky regions inside of the lath filled grains of the quenched material. A TEM image in figure 41 also shows small clear regions of the interior of the lath filled grains. As indicated in figure 41b-e SAD and CBED identify the clear regions as B2. Antiphase domains have not been found the B2 phase which may indicate that the B2 structure is stable at 1200°C. Based upon the combined evidence from alloys 15, 50 and 101 and other observations, it appears most likely that the T2 phase has a B2 structure at 1200°C.

The results indicate that a B2 structure existed at high temperature and decomposes to the $\alpha_2 + \gamma$ lath structure during cooling. Slowly cooled samples reveal only the lath structure in prior grains with each grain having a unidirectional lath structure. In addition, diffraction analysis indicates that a characteristic orientation relationship exists between α_2 and γ [$(0001)\alpha_2 \parallel (111)\gamma$ and $\langle 11\bar{2}0 \rangle \alpha_2 \parallel \langle 110 \rangle \gamma$] and furthermore another relationship holds between α_2 and the B2 phase [$\langle 11\bar{2}0 \rangle \alpha_2 \parallel \langle 111 \rangle B2$ and $(0001)\alpha_2 \parallel (110)B2$]. Therefore, it is quite reasonable that the a single grain of the B2 phase forms a unidirectional $\alpha_2 + \gamma$ lath structure. It should be noted that these observations are significant from several points of view. First, the usual formation of the $\alpha_2 + \gamma$ lath structure develops from a single phase α region upon cooling in binary Ti-Al alloys.

To date no one has reported the eutectoid transformation of the bcc related phase into the $\alpha_2 + \gamma$ lamellar structure. The unidirectional nature of this transformation is observed in each prior bcc grain. Beyond these microstructural observations it is noted that this particular microstructure is quite different in its mechanical behavior than the usual as-cast or annealed $\alpha_2 + \gamma$ binary alloys or alloys containing modest amounts of niobium. With only 10 at.% niobium this material is quite resilient and resistant to fracture under impact loading and exhibits plastic deformation. Microstructural evidence indicates twinning following deformation and work is underway on deformation and bend testing analysis.

These observations suggest a number of opportunities for microstructural control. One direction is the examination of a gradient cooling approach starting with an alloy based on the B2 phase in the T2 region. Annealing at high temperature will promote rapid grain growth of the bcc type phase so that under directional cooling a gradient grain growth will yield essentially single grains of the B2 phase and perhaps single crystals. The unidirectional lath structure that develops in the B2 phase will then, yield under controlled growth conditions, a unidirectional lath structure throughout a sample. Hence, with this approach an insitu composite of the $\alpha_2 + \gamma$ lath structure may be achieved. Initial results in collaboration with Dr. Mahapatra of NADC suggest that this approach is a viable one and will be pursued much further. A second avenue for microstructural control can be based upon the phase relationships

near the T2 region. Examination of figure 37 reveals the possibility of developing stable bcc + γ -TiAl phase mixtures. With alloys of varying composition in this two-phase region one could produce controlled volume fractions of the respective phases such as matrix of γ containing stable bcc precipitates. Alternatively, a bcc matrix containing a dispersion of γ precipitates could be produced with further transformation of the bcc matrix into the B8₂ dispersion phase. This approach would yield different size scales of dispersoid formation that have been suggested to be useful for strengthening with ultra fine dispersoids (i.e. B8₂ precipitates) and enhanced toughening and creep resistance with larger size dispersed constituents.

IV. Research Accomplishments in Other Alloy System

A. Nb-Al Alloy System

In an initial investigation of the potential for microstructural modification in Nb-Al through rapid solidification, drop tube processing was applied to a Nb-33 at.% Al alloy (σ -phase). This alloy, as can be seen in the equilibrium phase diagram of Figure 37, is at the peritectic composition for the σ -phase. As in TiAl, the growth kinetics for σ are estimated to be sluggish, based upon an α -factor of 2.46. Avoidance of σ -phase formation could lead to a variety of structural modifications including extension of the (bcc) Nb solid solution field, formation of a supersaturated Nb₃Al (cubic Al₁₅, β -W-type) phase, or a number of other metastable product structures.

X-ray diffraction analysis following drop tube processing under a H₂ gas environment, a summary of which is presented in Figure 43, revealed a variation in structure with powder size. In the finest powder (<20 μm) a combination of metastable diffraction peaks were observed, in addition to the equilibrium σ-phase pattern. A number of the diffraction peaks could be indexed as a (metastable) bcc phase, having a lattice parameter, *a*, of 0.329 nm. The origin of the remaining x-ray peaks is currently under investigation. As the powder size increased above 20 μm, the intensity of the metastable peaks, with respect to those of the equilibrium structure, decreased abruptly. Above approximately 60 μm, x-ray analysis indicated the presence of only the equilibrium σ-phase.

Microstructural examination of the <20 μm drop tube processed powder, as illustrated in Figure 44, revealed a variation in the microstructural scale and morphology along each powder cross-section. The finest powder in the <20 μm class consisted generally of a fine two-phase mixture (Figure 44a), with the second phase appearing as a fine dispersoid in the matrix. The spacing of the second phase increased across the particle section, as is often observed during the recalescence period of solidification. The larger powder in the <20 μm class often contained a hemispherical region adjacent to the droplet surface similar to the fine powder microstructure, however, this region was bounded by a dendritic two-phase zone which occupied the remaining droplet volume (Figure 44b). The 20-37 μm powder contained cellular/dendritic microstructures, as illustrated in

Figure 45. The hemispherical growth morphology and variation in dendrite spacing across the particle (Figure 45a) is again typical of recalescence in an undercooled melt. Many of the particles showed evidence of solid state decomposition in the form of plate-like precipitates which originated at the cell boundaries (Figure 45b).

While the microstructure development pathway in the σ -phase powder appears to be complex, the initial x-ray/microstructural analysis implies that a metastable bcc structure forms initially in the undercooled melt. Based on a metastable phase diagram, shown in Figure 46, partitionless formation of the bcc phase requires an undercooling of only approximately 300°C ($0.13T_1$). The kinetics of decomposition of the bcc structure appear to be rapid, being only partially suppressed even in the smallest powder. The x-ray evidence of a second metastable phase may represent an intermediate decomposition product or a metastable solid formed at lower undercooling/growth velocities in the later stage of recalescence.

B. Nb-Cr Alloy System

The niobium-chromium alloy system offers interesting potential for composite development, alternate phase formation and high temperature applications. The intermetallic compound (NbCr_2) has a stable, partially ordered phase field (β') up to $T = 1588^{\circ}\text{C}$ (Figure 47). Also, in the phase diagram of Figure 47, it is apparent that at liquid undercoolings of approximately 200 K, the β' phase can form from the melt instead of the brittle

hexagonal phase (β). Moreover, with even higher liquid undercoolings the formation of a disordered bcc phase is thermodynamically possible.

In order to evaluate the structural development in NbCr_2 alloys, drop tube processing has been utilized along with splat quenching treatments. Initial results on the containerless processing indicate multiple phase selections and/or evolutions. For drop tube processed powder less than $38 \mu\text{m}$, x-ray diffraction indicated the existence of β and β' in addition to an unknown alternate phase. X-ray diffraction pattern from fine Nb-52.7 wt. % Cr powder after drop tube processing is shown in figure 48. Splat quenching consists of levitating 60 mg samples, melting the charge, and splat quenching the falling sphere between copper anvils so that segregation is reduced to a fine, uniform scale.

Results from splat quenching again illustrated alternate structural evolutions in the Nb-Cr system (Figure 49). The β and β' phases were again present in the structure as was the case for drop tube processing, but in addition, other unknown phases have emerged which are currently being assessed. Moreover, the finely dispersed structures in the powder flakes were relatively stable with heat treatment. The samples were heat treated at 600°C for 1 hour with a 1 hour ramp up and ramp down time. The resultant diffraction scan is illustrated in Figure 49b and reveals no significant change during the thermal cycle.

In order to promote the formation of the disordered bcc phase at the intermetallic composition, small amounts of titanium were added to the splat quenches samples. Titanium additions to both

niobium and chromium promote the formation of a disordered bcc phase from the melt. The resultant effect on the phase selection of a $\text{NbCr}_2+10 \text{ wt}\% \text{ Ti}$ alloy is shown in the x-ray diffraction scan of Figure 50. A substantial amount of a disordered bcc phase was apparent in this structure. Moreover, the bcc splat samples showed some ductility compared to the ordered phase structure. The lattice parameter of the bcc phase was $a_0 = 3.07\text{\AA}$, and using Vegard's Law between the Nb and Cr phase at the intermetallic composition, the lattice parameter should be $a_0 = 3.03\text{\AA}$. In addition, heat treatment of this alloy at 600°C for 1 and 6 hours showed no significant sign of decomposition. Further studies are in progress to optimize the bcc product yield and to examine the thermal stability for consolidation treatments.

C. Al-V Alloy System

The aluminum-vanadium alloy under preliminary investigation is the Al_8V_5 intermetallic compounds at Al-56 wt% as shown in the phase diagram of figure 51. The ingots are produced via arc-melting and homogenized at 1100°C for 10 days. Crushed powder from the ingot is then drop tube processed in a 1 atm $\text{He-2}\% \text{H}_2$ environment, and the attempted superheat is at least 50°C . Analysis was performed by room temperature x-ray diffraction, scanning electron microscopy (SEM) and differential thermal analysis (DTA).

SEM of the arc-melted, homogenized, and drop tube processed powder illustrated different microstructures for the individual treatments. The arc-melted structure is dendritic with the

possibility of a minimal amount of a third phase (perhaps ϵ), the homogenized structure is essentially featureless, and the drop tube processed powder structure is rather varied with powder size. A range of morphologies and phases are apparent, and a transitional effect with size (between 10 and 75 μm) occurs which is consistent with nucleant isolation distributions.

X-ray diffractometer scans were done on the arc-melted, homogenized, and drop tube processed powder. Peak separation of the V-rich dendrites and the ζ phase in the arc-melted stage is difficult because the lattice parameter difference between the disordered and ordered phase is a factor of three, thus causing overlap of the peaks. Therefore, a comparison between the standard homogenized powder (100% ζ) and the arc-melted powder is being attempted via deconvolution techniques to access the relative abundance of phases in the arc-melted sample. With the deconvolution analysis, the abundance of phases in the drop tube processed powder can also be evaluated. With decreasing powder size, however, non-equilibrium peaks emerge. These peaks disappear with heat treatment in DTA cycles, and the resultant diffraction scan becomes identical to that of the homogenized powder.

Although x-ray and SEM analysis appear to be in reasonable agreement (albeit not completely defined), DTA offers an interesting addition to the evaluation. Drop tube processed powders examined thus far (less than 63 μm) illustrate transformations at temperatures between 600°C and 1400°C. During heating, endotherms at $\sim 685^\circ\text{C}$, $\sim 1179^\circ\text{C}$ and $\sim 1345^\circ\text{C}$ were detected,

as well as the corresponding exotherms upon cooling. No decomposition exotherms at temperatures below 600°C have been searched for yet, and expanded scale analysis from 650°C and 750°C is needed. Although the repeatable 685°C and 1345°C transitions can be explained with a large composition shift (either by segregation or potentially by vanadium loss), the 1170°C transition is not apparent on the Al-V binary phase diagram, but a reaction occurs in this temperature range in the vanadium-oxygen system.

In review of the Al-V binary system, many questions are unanswered, however, the system illustrated variable structural evolution that warrant further investigation. The structure indicates two distinct morphologies with decreasing powder size and evidence of microstructural features characteristic of recalescence. These observations suggest the potential for undercooling and alternative phase selection. X-ray diffraction evidence supports the existence of metastable pathways with finer powders. DTA suggests one of two possibilities; large segregation could occur during drop tube processing or vanadium could be oxidizing. It is interesting to note that the vanadium-oxygen system has a reaction at $\sim 1180^{\circ}\text{C}$, but x-ray analysis (with limited sensitivity to finely dispersed phases) shows no indication of any other phases than the ζ phase after the DTA cycles.

V. Summary Highlights

- The phase selection, solidification pathways and thermal stability of solidification products have been examined in intermetallic alloys in the Ti-Al, Nb-Cr and Ti-Al-Nb systems.

- A detailed study of powder solidification following atomization and drop tube containerless processing has been performed in binary Ti-Al alloys. The two most significant variables were found to be alloy composition and powder size.

- In Ti-Al alloys at the Ti_3Al composition, solidification occurred through the formation of β (A2) from the melt followed by a martensitic transformation to a hexagonal α' structure and then a partial ordering to α_2 (DO₁₉). As the Al content was increased to 40 at. % the finest powder (<40 μ m) processed under He gas solidified as α (followed by ordering to α_2), while larger powders formed as β from the melt. From 48 to 52 at. % Al virtually all powders solidified initially as α , with γ forming near the end of solidification. In each of these alloys, as the powder size increased the volume fraction of γ forming in the interdendritic regions increased. At 55 at. % Al, the finest powder processed under He formed a small amount of α , while the remaining samples solidified as γ from the melt.

- An analysis of the microstructure development in powders in terms of the revised phase diagram and phase selection kinetics yields estimates of melt undercooling during structure

formation. For example the observation of α formation in a Ti-40 at. % Al alloys indicates the operation of a metastable solidification pathway which requires a certain minimum level of undercooling. From an analysis of the T_0 curves for L/ α and L/ β phase pairings a minimum undercooling in excess of 50°C is found for this alloy. For Al contents between about 45 to 52 at. % Al both the phase diagram and the T_0 curve analysis indicate a close balance of phase stability between the bcc and hcp structures. This balance represents an opportunity for manipulating product structure through controlled processing. A start in the development of controlled processing treatments and analysis has been established in this program.

- The thermal stability of the metastable α_2 phase in the high Al content alloys has been defined in DTA studies. Two major decomposition reactions at 640°C and 725°C have been established for the development of a lamellar $\alpha_2 + \gamma$ morphology. Interestingly, most of the coarse atomized powder sizes decomposed at 725°C. In drop tube processed powder only the high temperature decomposition reaction was detected.

- Based on TEM studies the decomposition reaction yields the following low energy orientation relationships between α_2 and γ :

$$(0001)-\alpha_2 \parallel (111)-\gamma$$

$$[\bar{2}110]-\alpha_2 \parallel \langle 110 \rangle-\gamma$$

- The establishment of a low energy orientation relationship

during the decomposition of the metastable supersaturated α_2 to an equilibrium $\gamma + \alpha_2$ lamellar mixture provides a key element to account for the observed decomposition kinetics. A rate limiting step based upon the formation of new γ plates within the α_2 phase has been identified. With this model the rate of decomposition is dependent on the relative amounts of α_2 / γ interphase area and thus upon the scale of the solidification microstructure. As a result a finer dendritic microstructure will decompose at a lower temperature than a coarse cellular structure for a comparable rate. With this model the activation energy for the decomposition reaction has been estimated to be about 1×10^5 J/mole, but a further more detailed examination of the kinetics is worthwhile.

- As a result of separate investigations on the phase equilibria of Ti-Al-Nb alloys, it has been determined that the phase equilibria for Ti-rich alloys is dominated by bcc-type phases. Due to the evolution of novel microstructures during decomposition of the high temperature phases upon cooling the transformation reactions have been examined for selected alloys. An alloy of $\text{Ti}_{45}\text{Al}_{44}\text{Nb}_{11}$ appears to be a B2 (CsCl) structure at 1200°C and develops a unidirectional α_2 / γ lamellar structure upon cooling. TEM investigation of samples quenched from 1200°C has revealed that the B2, α_2 and γ phases exhibit orientation relationships with respect to each other. Therefore, it appears that a single grain of B2 forms a packet of the unidirectional $\alpha_2 + \gamma$ lamellar structure. This result represents the discovery of

a new reaction mechanism (i.e. $B2 \Rightarrow \gamma + \alpha_2$) for development of the lamellar structure that is not available in binary Ti-Al alloys. The development of orientation relationships between three phases involved in a transformation is also rather rare.

- These observations suggest a number of opportunities for microstructural control that are under active development. In one approach, a directional transformation in a steep temperature gradient is being used to create single grain B2 which then transforms to a unidirectional $\alpha_2 + \gamma$ lamellar structure. In effect this method has yielded an in-situ composite which has also exhibited exceptional impact resistance. Another approach is directed towards the development of two phase mixtures such as $\gamma + \beta$ structures. Again the initial two phase structure is modified upon cooling from high temperature to allow for the in-situ development of various size scales of dispersed phases to enhance toughness and creep resistance.

- In the Nb-Al system supersaturation of the primary Nb-rich bcc solid solution has been reported in a number of studies to extend out to about Nb_3Al following rapid solidification. With increasing Al content formation of a σ phase (Nb_2Al) develops and yields reduced levels supersaturation. Based upon a thermodynamic analysis it appears that a metastable bcc phase can also develop near the σ phase composition. Following containerless processing evidence for formation of the predicted bcc phase was found, but the pathway is complicated by various

solid state reactions that are being resolved currently.

- A thermodynamic analysis of the Nb-Cr system has indicated that if the equilibrium Laves phases at the composition NbCr_2 can be suppressed a wide range of metastable bcc phase is possible. Following solidification processing a wide range of bcc phase was found. The addition of 10 wt.% Ti served to promote bcc phase formation. In contrast to Laves phases the bcc phase was ductile. Moreover, following decomposition of the metastable structure a fine scale bcc + Laves phase mixture resulted which is under further study.

Ti-Al BINARY SYSTEM

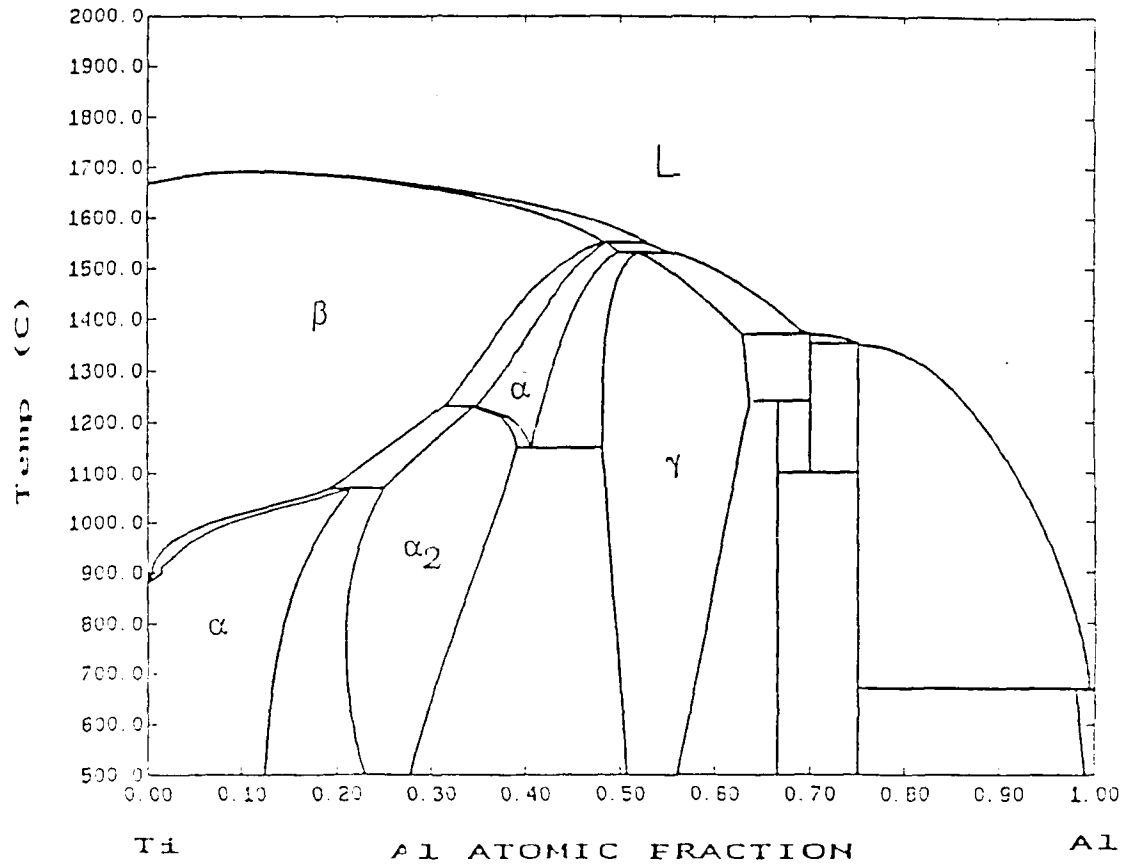
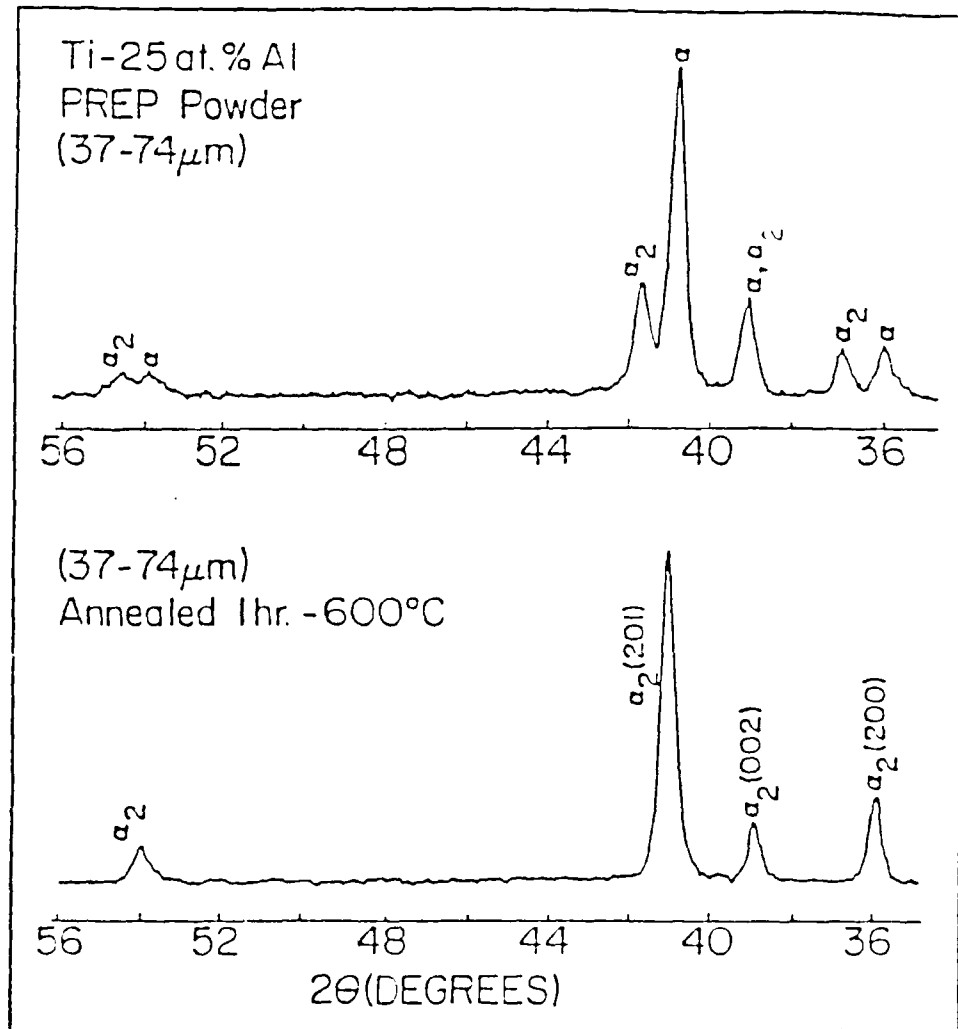


Figure 1. Revised Ti-Al binary phase diagram based upon thermodynamic modeling analysis of the current research at the University of Wisconsin-Madison.

Figure 2. Ti₃Al X-ray diffraction data.

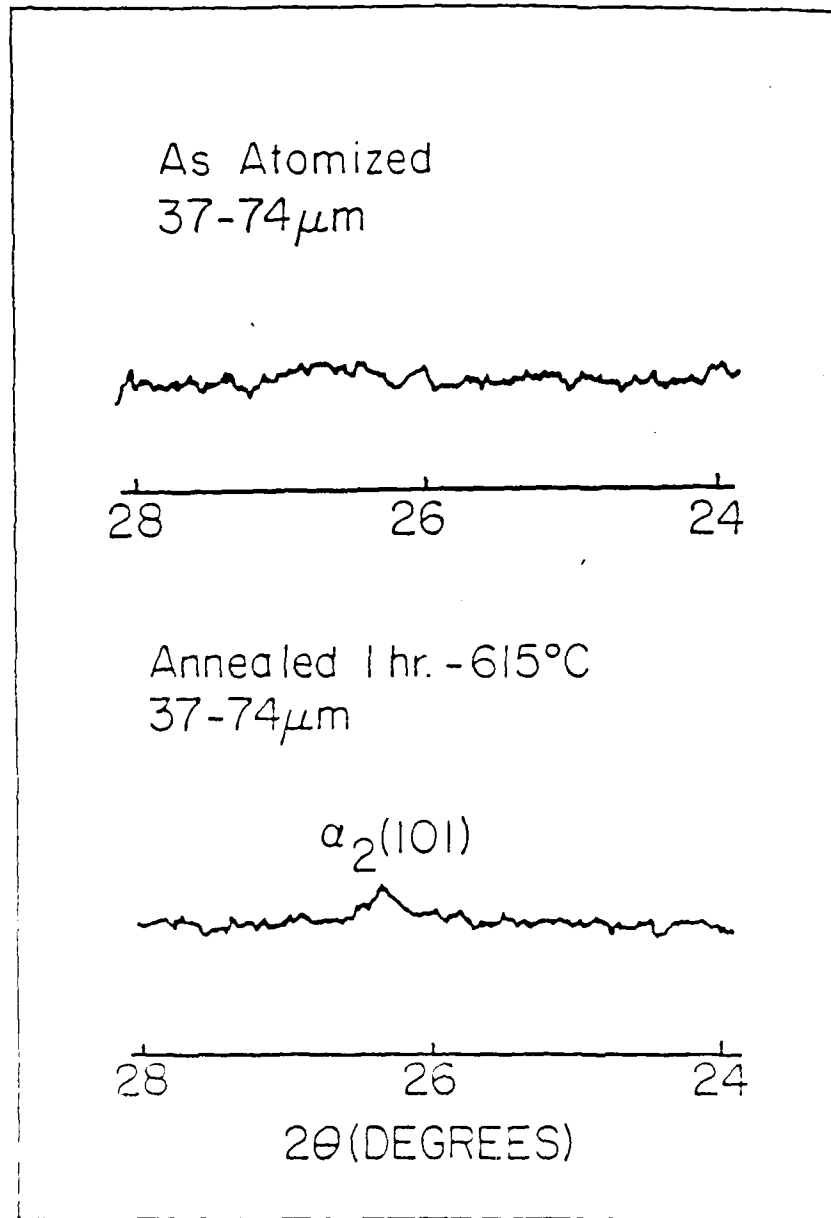


Figure 3. Comparison of x-ray diffraction patterns for Ti₃Al (37-74μm) in the as-atomized and annealed (1 h at 600°C) showing the development of superlattice (101) reflections for the α₂ phase.

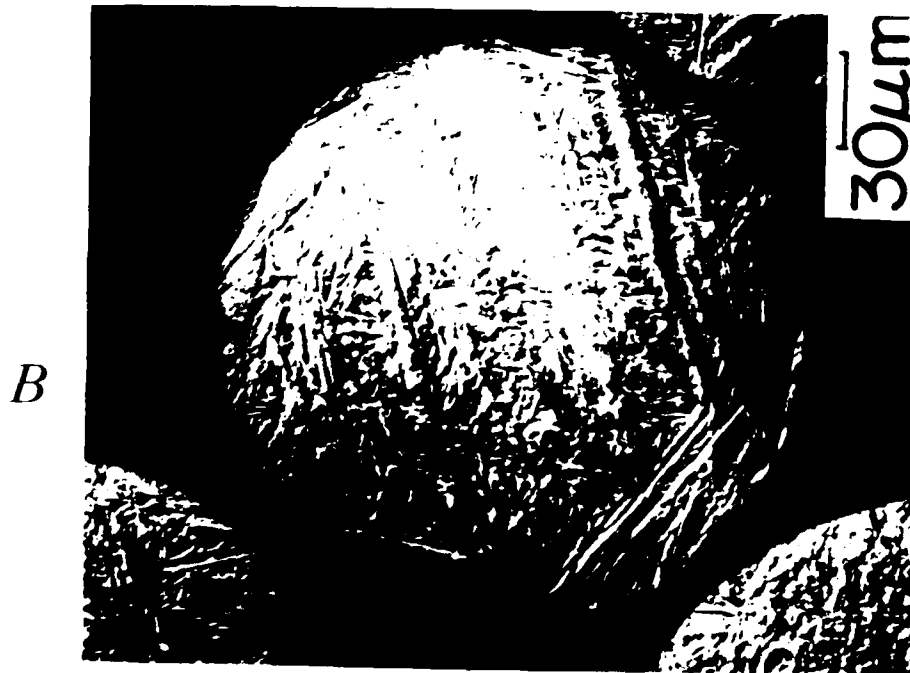
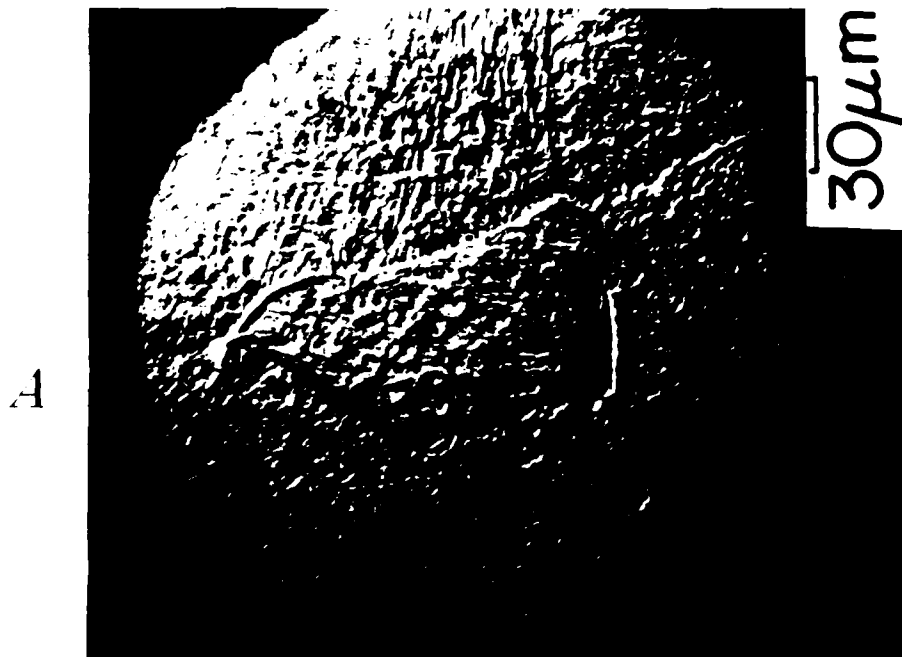


Figure 4. a) Ti₃Al martensitic structure with prior beta grain boundaries; b) Ti₃Al martensitic structure with inclined acicular plates.

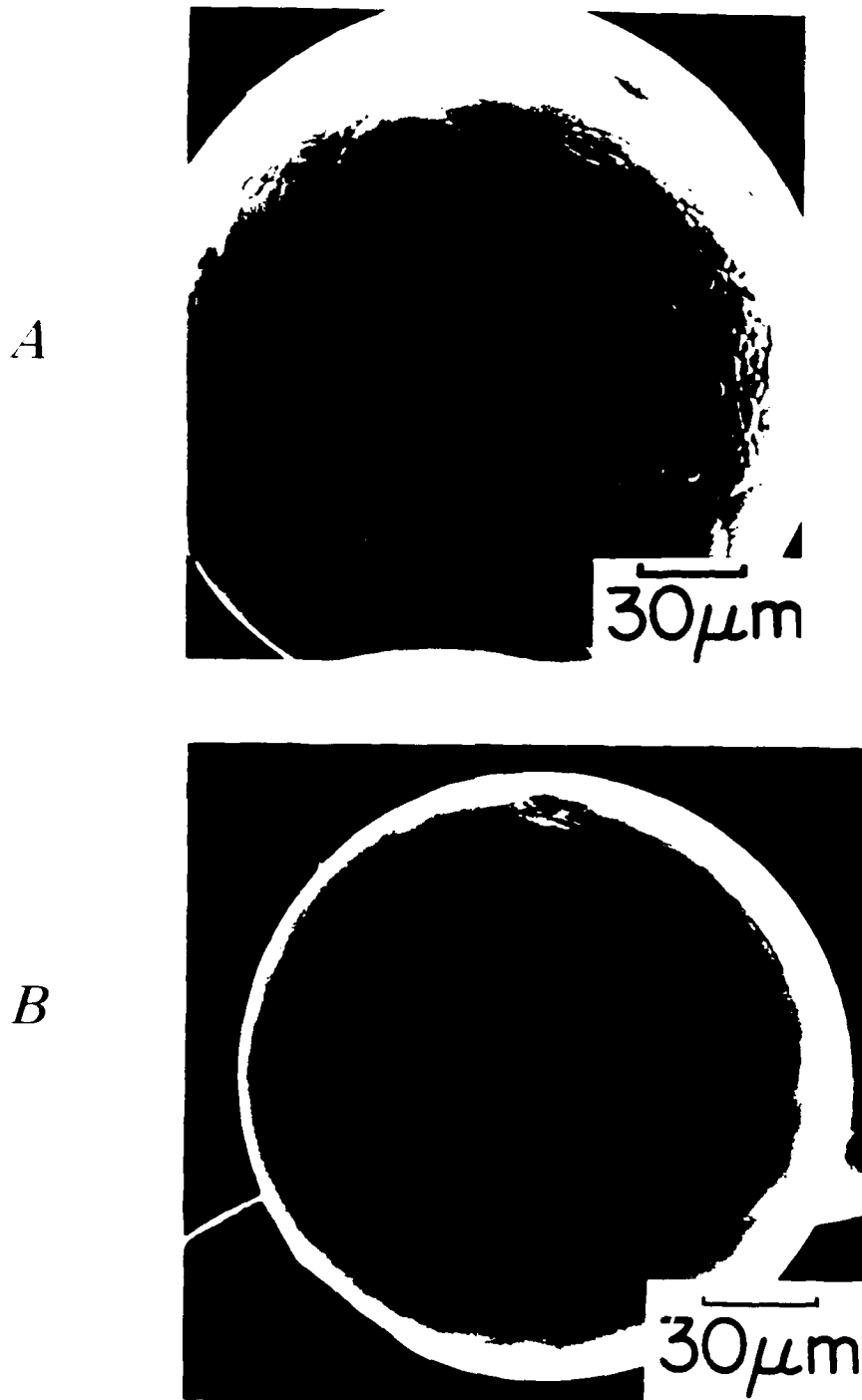


Figure 5. a) Surface Ti_3Al with partial cellular-dendritic pattern; b) smooth surface Ti_3Al with martensitic texture visible.

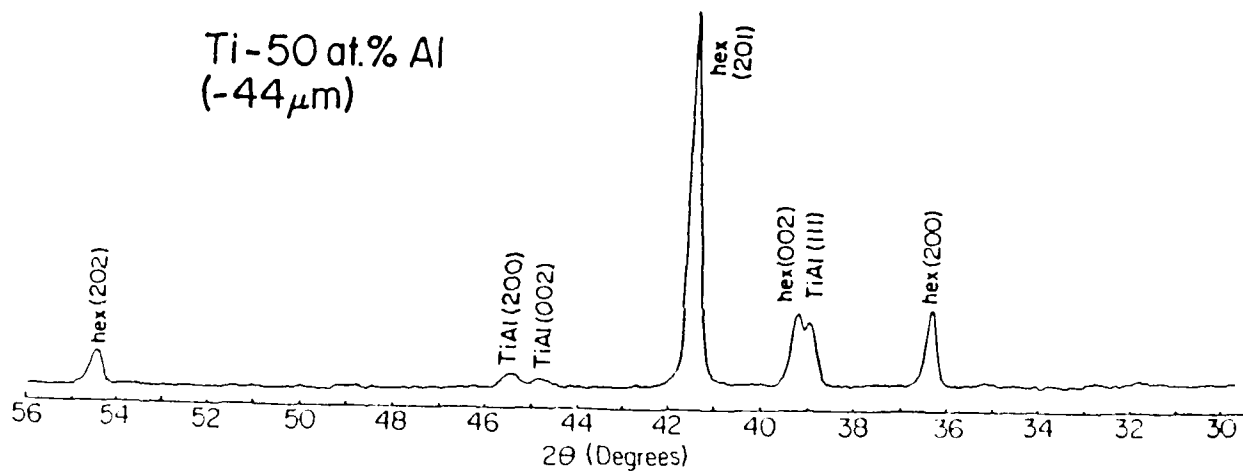


Figure 6. X-ray diffraction pattern for <44 μ m TiAl powder showing dominance of metastable α_2 structure.

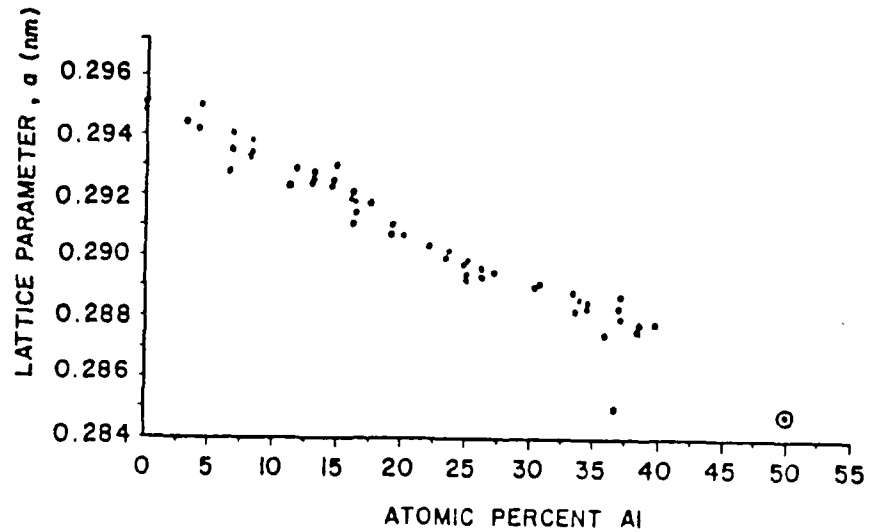
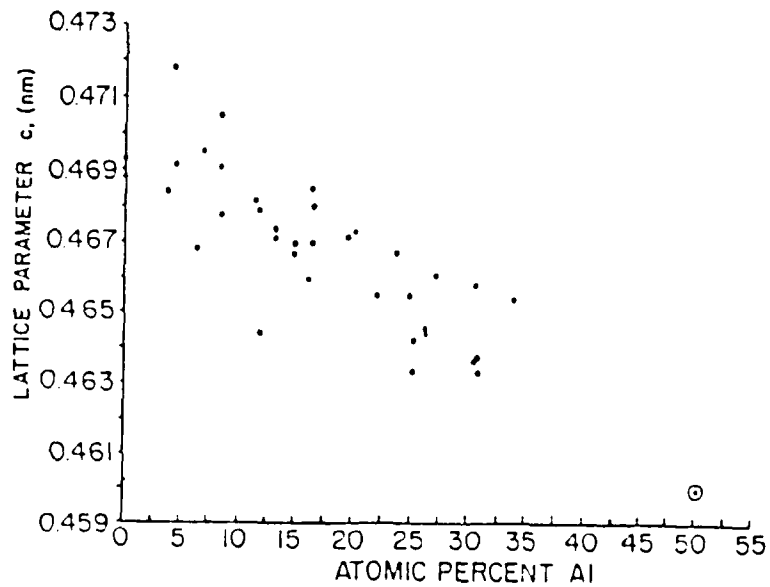
LATTICE PARAMETER (a , nm) FOR HEXAGONAL CRYSTAL STRUCTURELATTICE PARAMETER (c , nm) FOR HEXAGONAL CRYSTAL STRUCTURE

Figure 7. Summary of lattice parameter data for α and α_2 showing value for metastable α_2 produced at the equiatomic composition. Note: data standardized to disordered hcp values through a_0 (ordered) equals $2a_0$ (disordered).

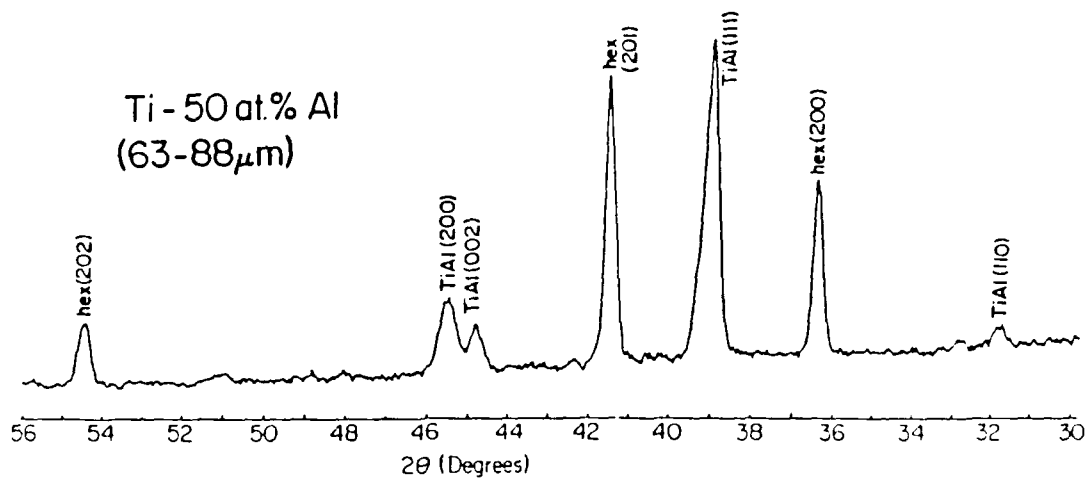


Figure 8. X-ray diffraction pattern of 63-88 μ m TiAl powder.

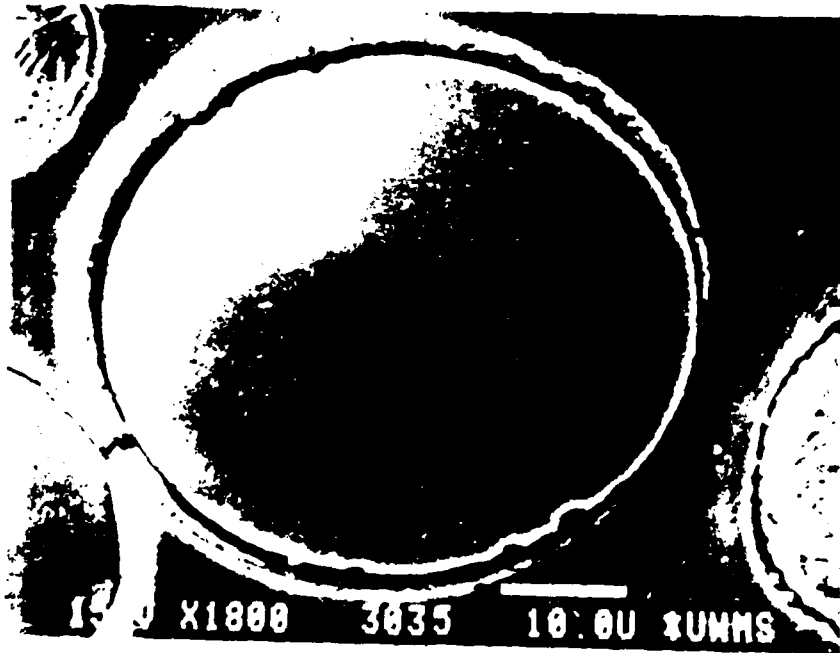
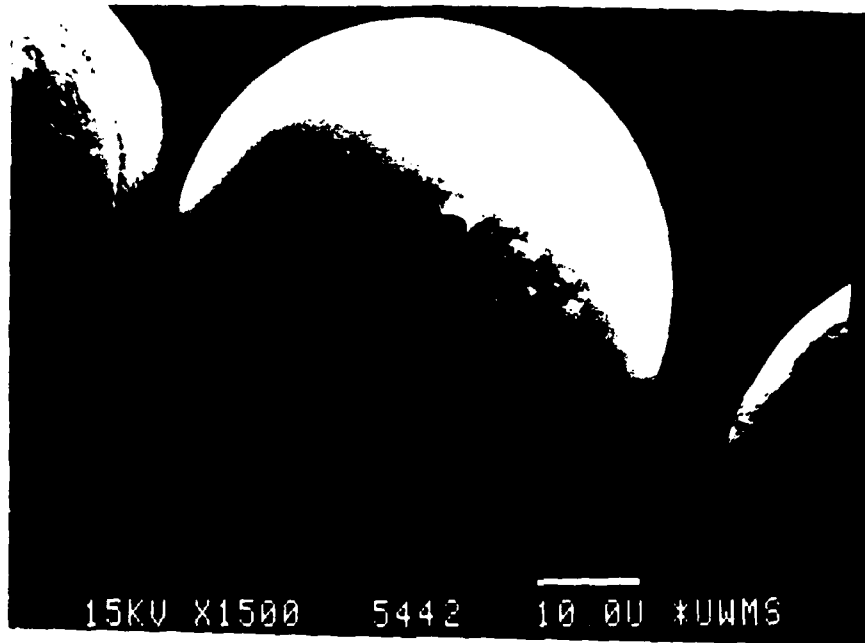


Figure 9. SEM micrographs showing single phase (metastable α_2) particles of equiatomic composition.

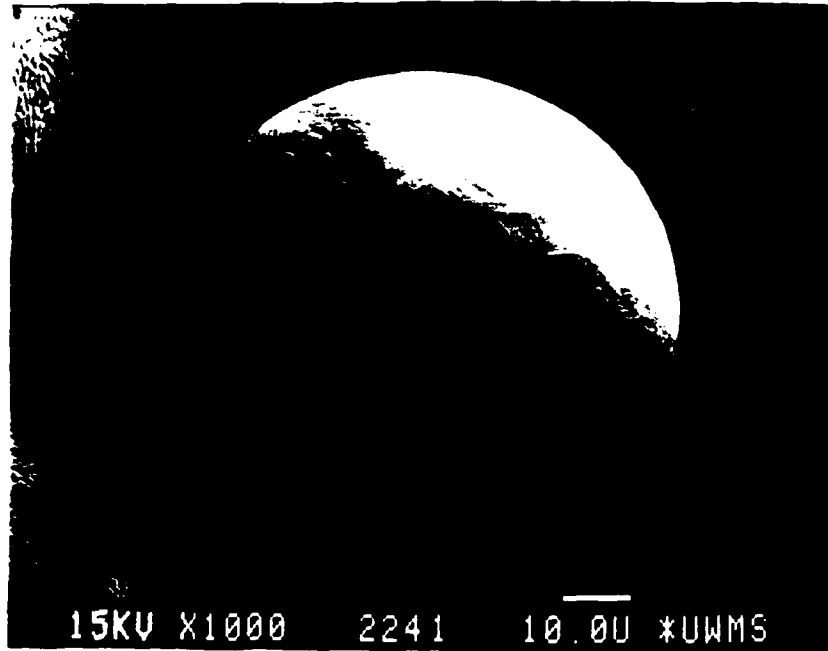


Figure 10. SEM micrograph showing single phase martensitic particle of equiatomic composition.

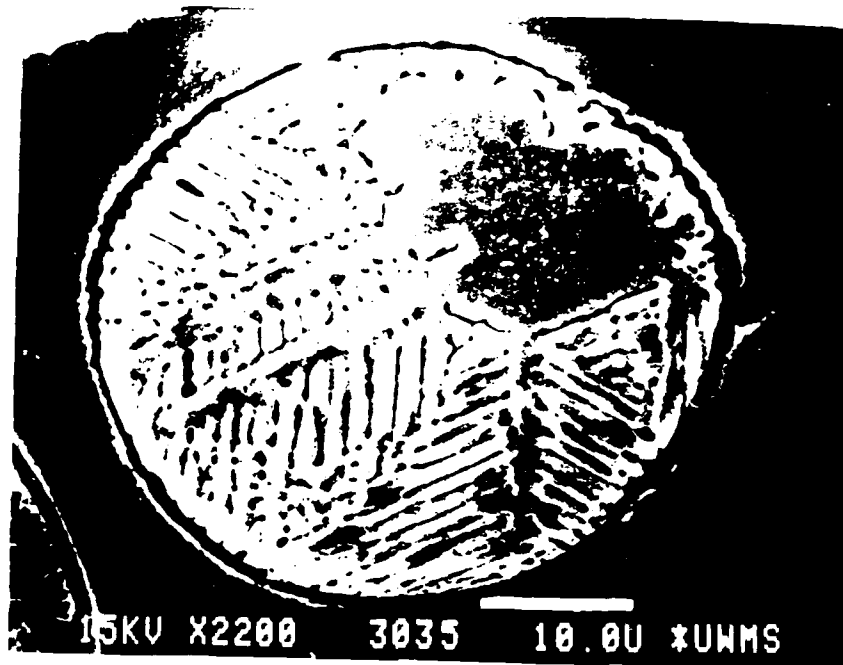


Figure 11. SEM micrographs of dual phase ($\alpha_2 + \text{TiAl}$) particles of equiatomic composition. Note: initial phase morphology on particle perimeter denoted by "A".

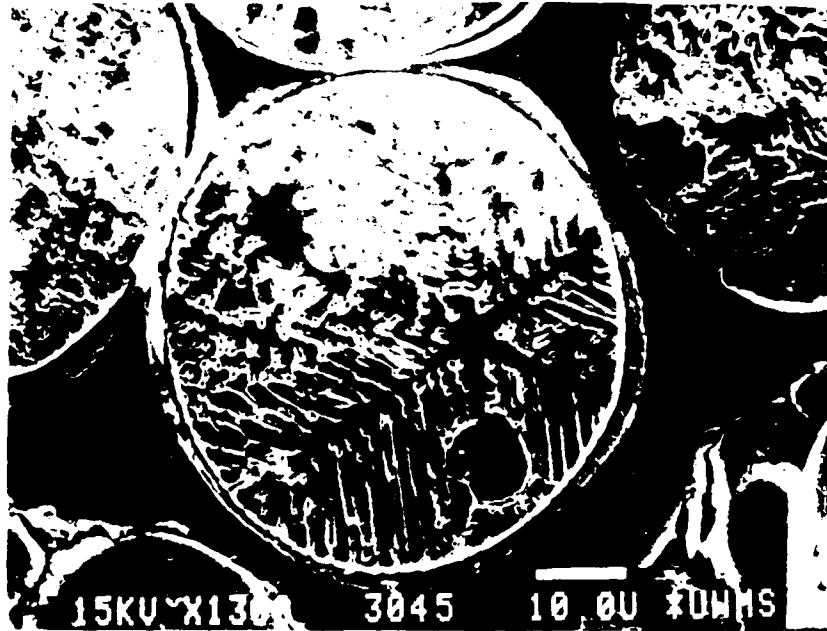


Figure 12. SEM micrograph showing six fold rotational symmetry which is characteristic of a hcp solidification morphology.

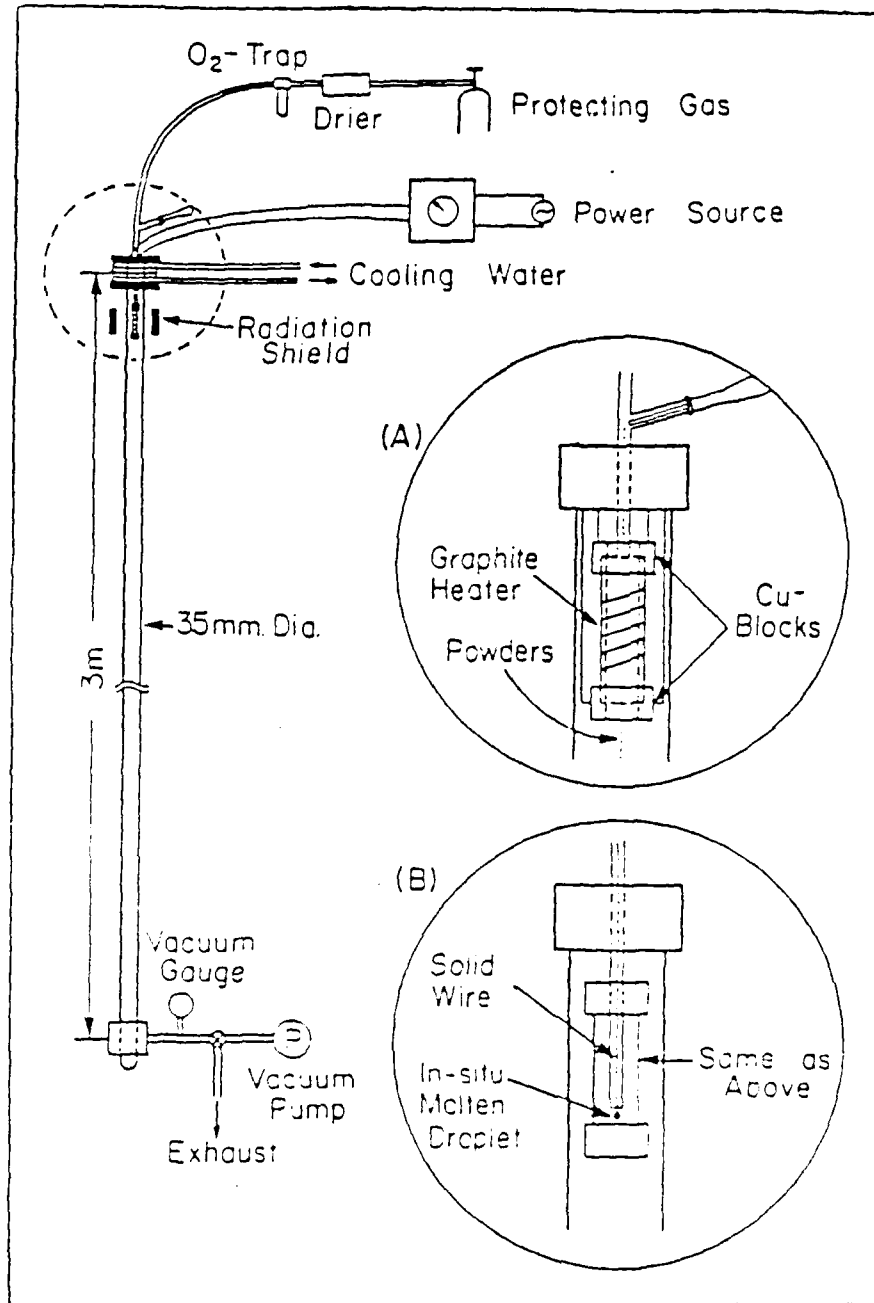


Figure 13. Schematic illustration of laboratory scale drop tube processing apparatus.

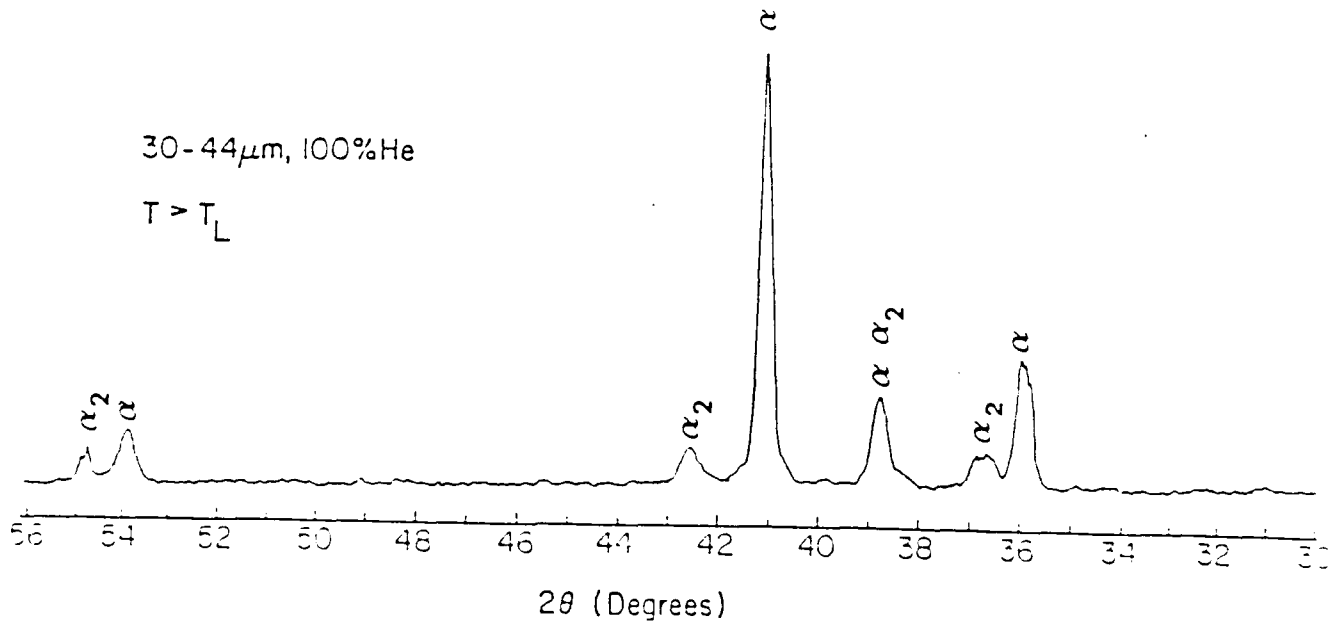


Figure 14. X-ray diffraction pattern for drop tube processed Ti-31 at. % powder, heated above the liquidus temperature.



Figure 15. SEM micrograph showing acicular martensitic structure in drop tube processed (He) Ti-31 at. % Al powder, heated above the liquidus temperature.

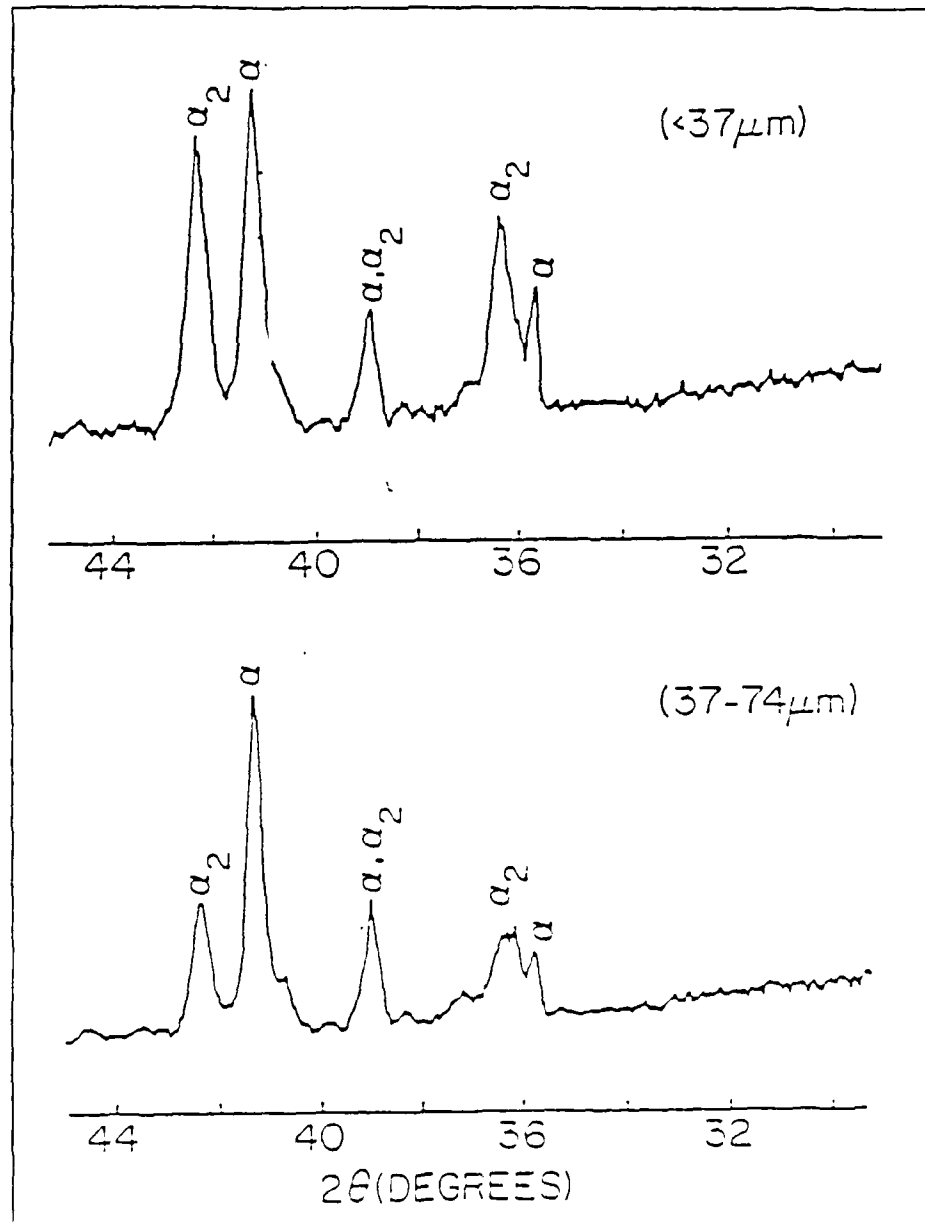


Figure 16. X-ray diffraction patterns for drop tube processed (He) Ti-40 At. % Al powder.

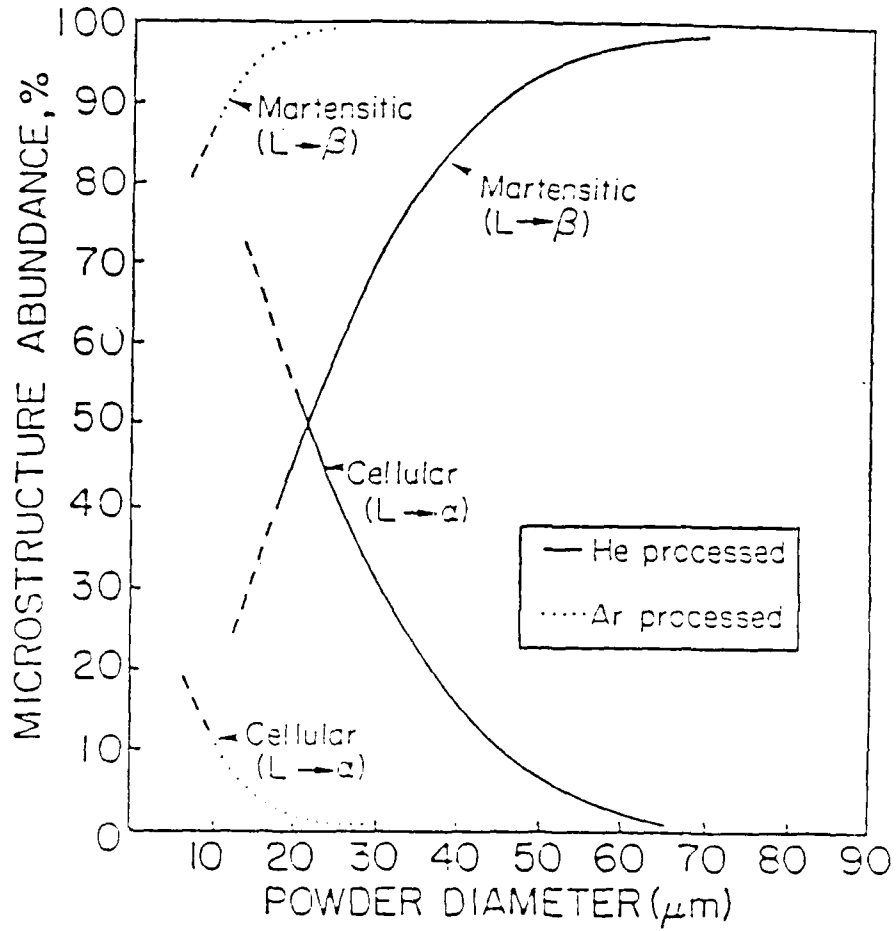


Figure 17. Summary of microstructural analysis for drop tube processed Ti-40 at. % Al powder.

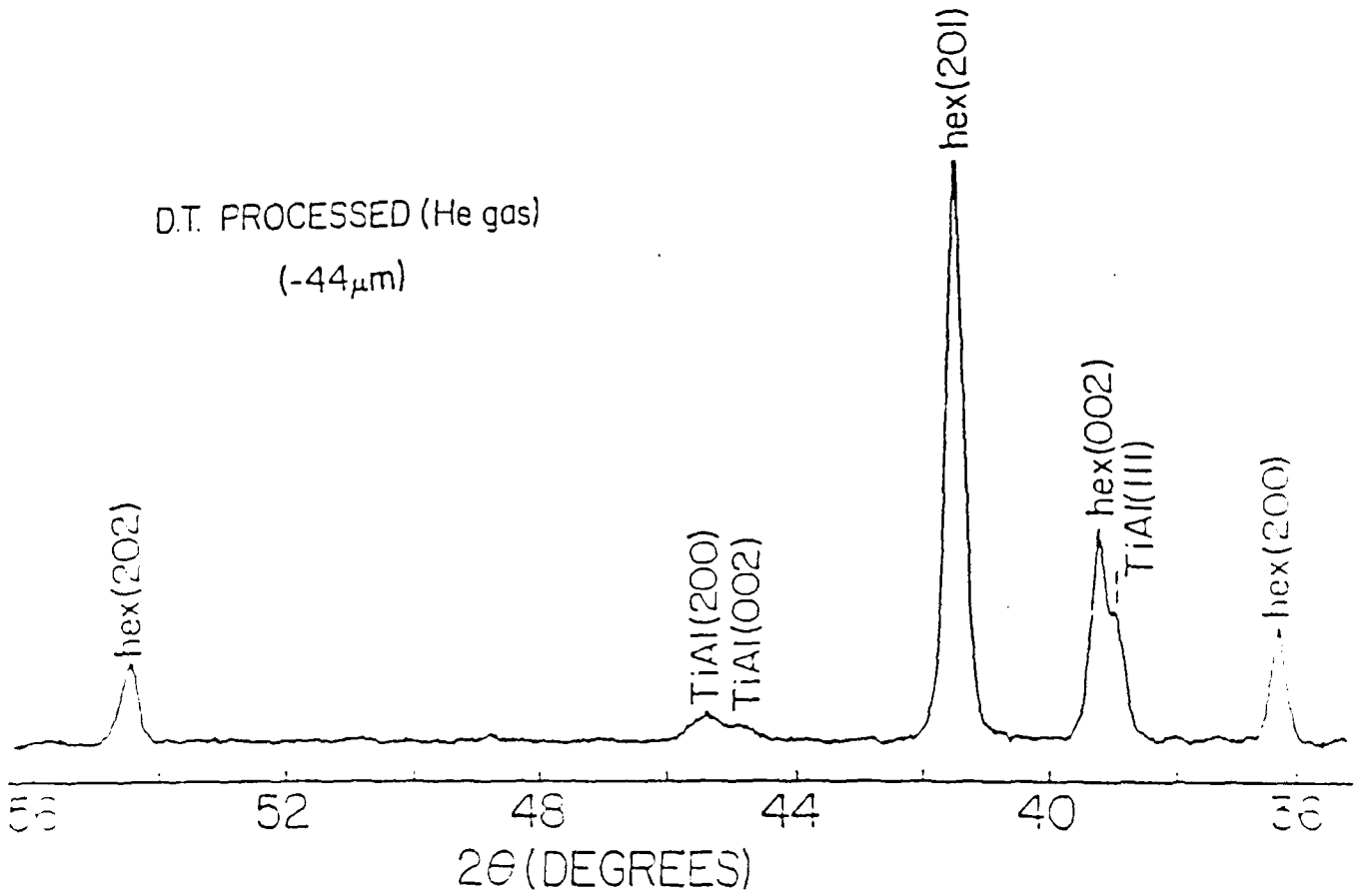


Figure 18. X-ray diffraction pattern for drop tube processed (He) Ti-48 at. % Al powder.

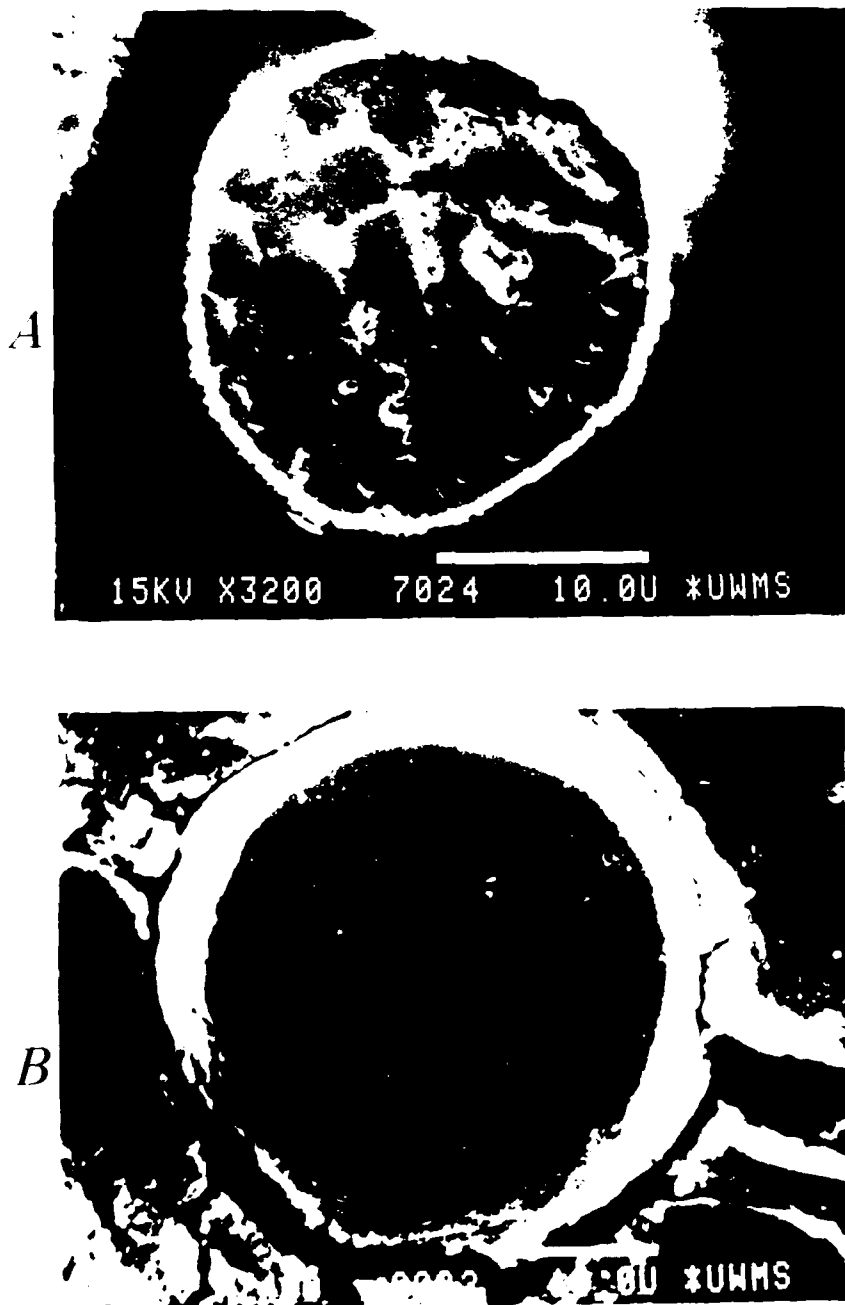


Figure 19. SEM micrographs showing a) cellular and b) single phase microstructures for drop tube processed Ti-48 at. % Al powder.

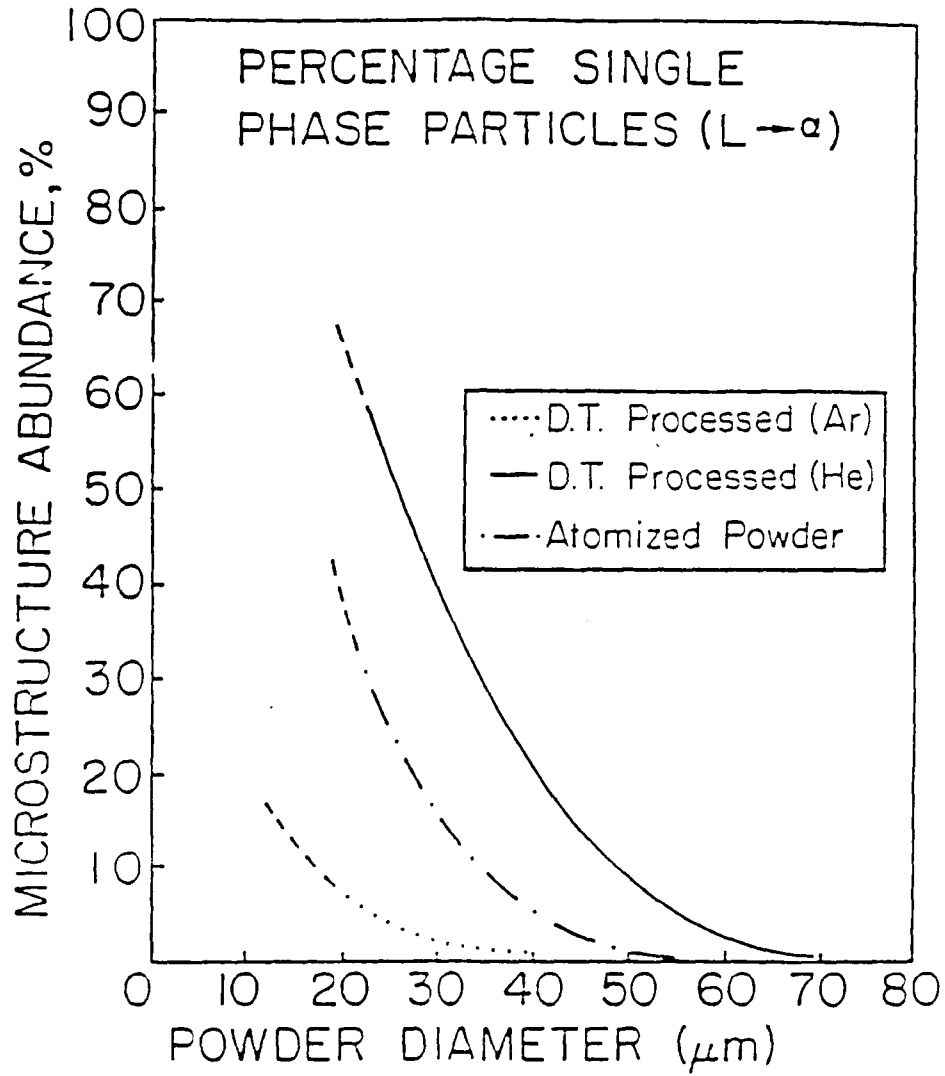


Figure 20. Summary of single phase (α_2) microstructural abundance for drop tube processed and atomized Ti-48 at. % Al powder.

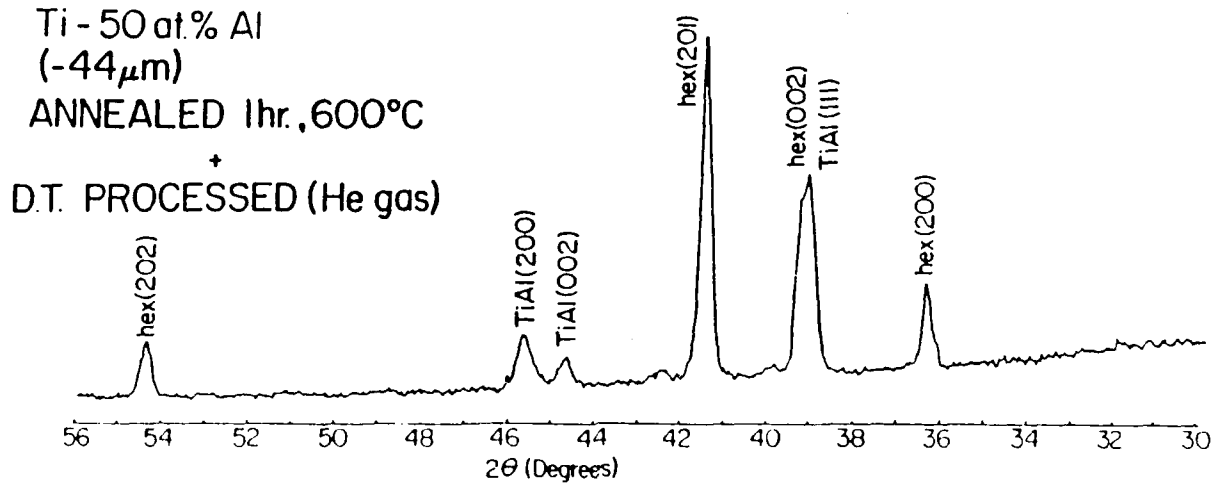


Figure 21. X-ray diffraction pattern showing presence of metastable α_2 and equilibrium TiAl in drop tube processed Ti-50 at. % Al powder (<44 μ m).



Figure 22. SEM micrographs showing dual phase (α_2 + TiAl) structure developed during drop tube processing of Ti-50 at. % Al powder.



Figure 23. SEM micrograph showing cellular TiAl structure in drop tube processed Ti-55 at. % Al powder.



Figure 24. As-solidified microstructure of Ti-56 at. % Al melt spun ribbon in a bright field image.

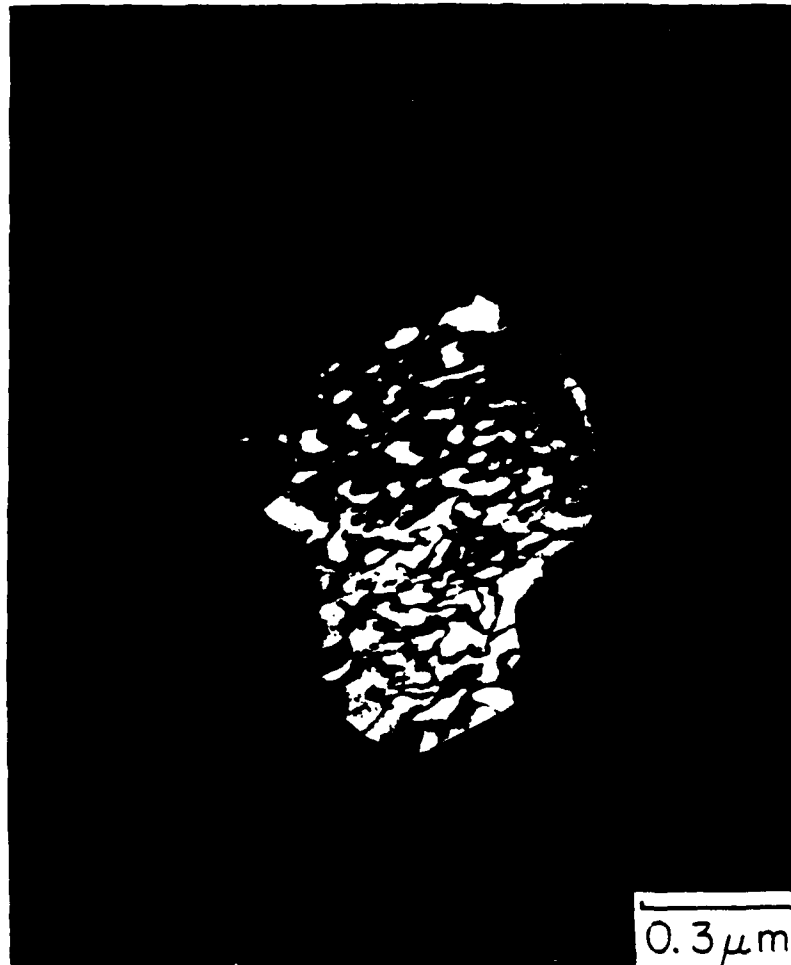


Figure 25. Dark field image of the DO₁₉ phase using a superlattice reflection. Note fine antiphase domains indicating ordering occurs in the solid-state (i. e. to α_2).

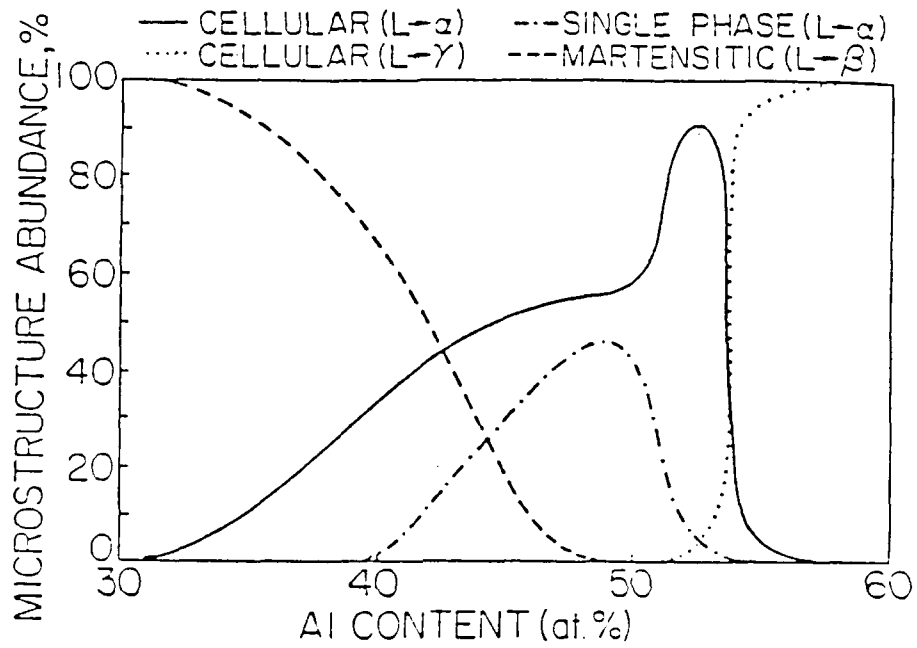


Figure 26. Summary of microstructural variation with Al content in "fine" drop tube processed (He) powder.

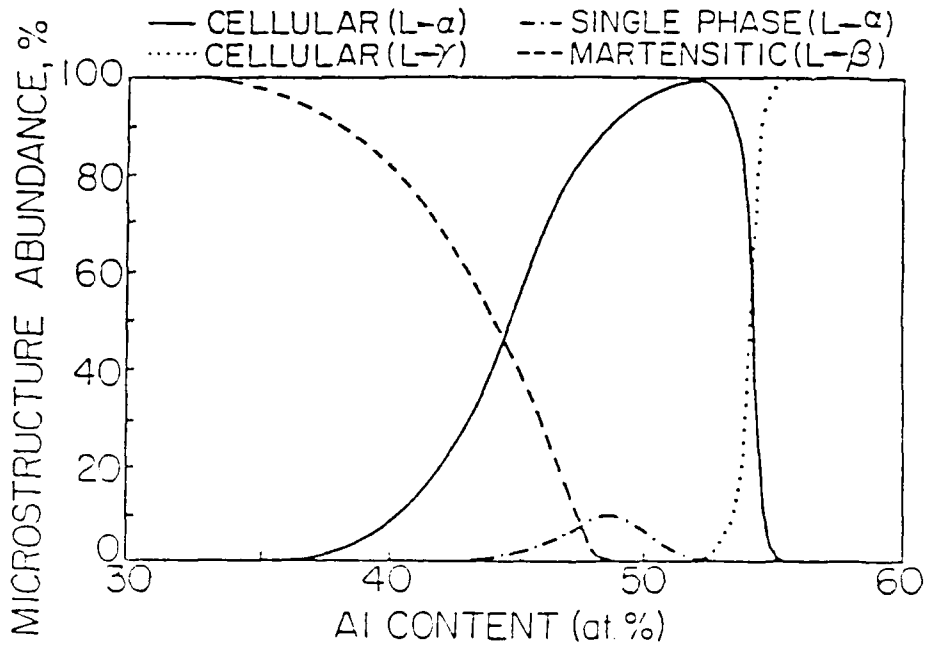


Figure 27. Summary of microstructural variation with Al content in "coarse" drop tube processed (He) powder.

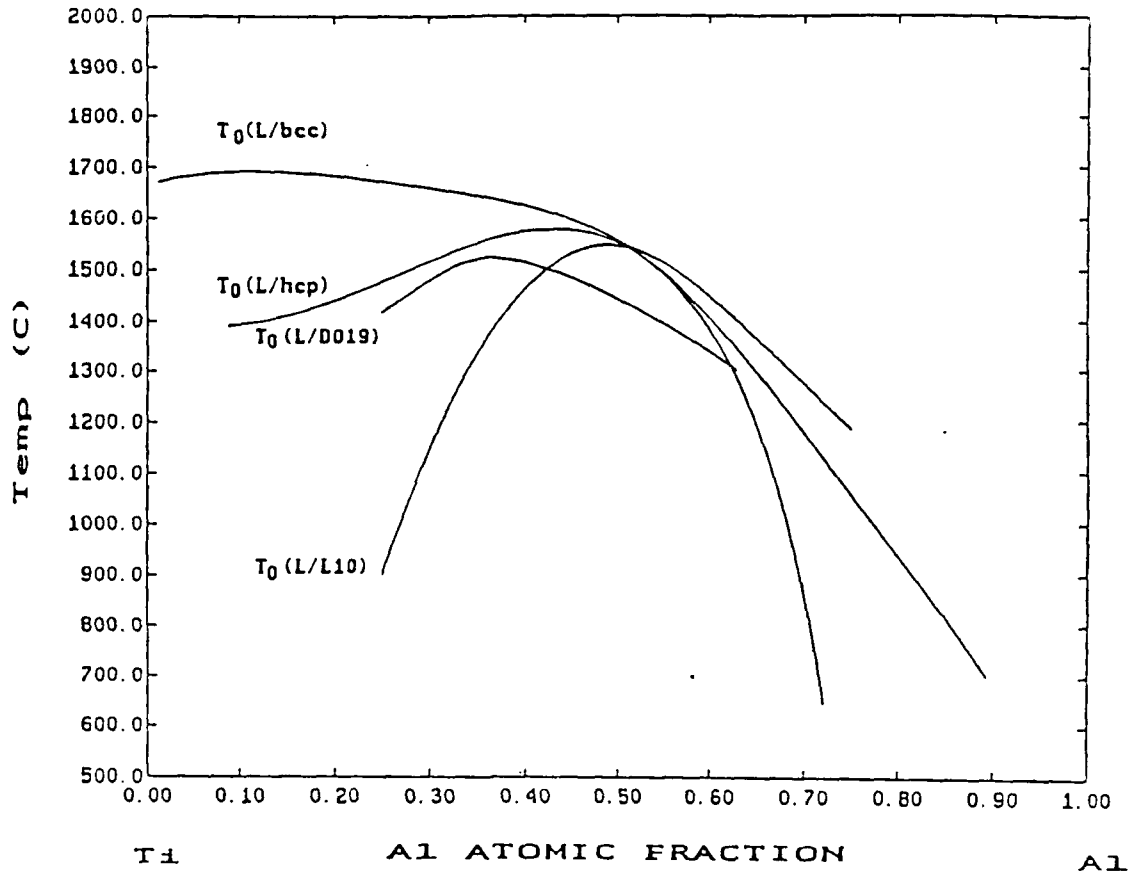


Figure 28. Calculated T_0 curves for several phases observed during rapid solidification processing of Ti-Al alloys. The calculation is based on the thermodynamic model analysis that was used to develop the phase diagram in figure 1.

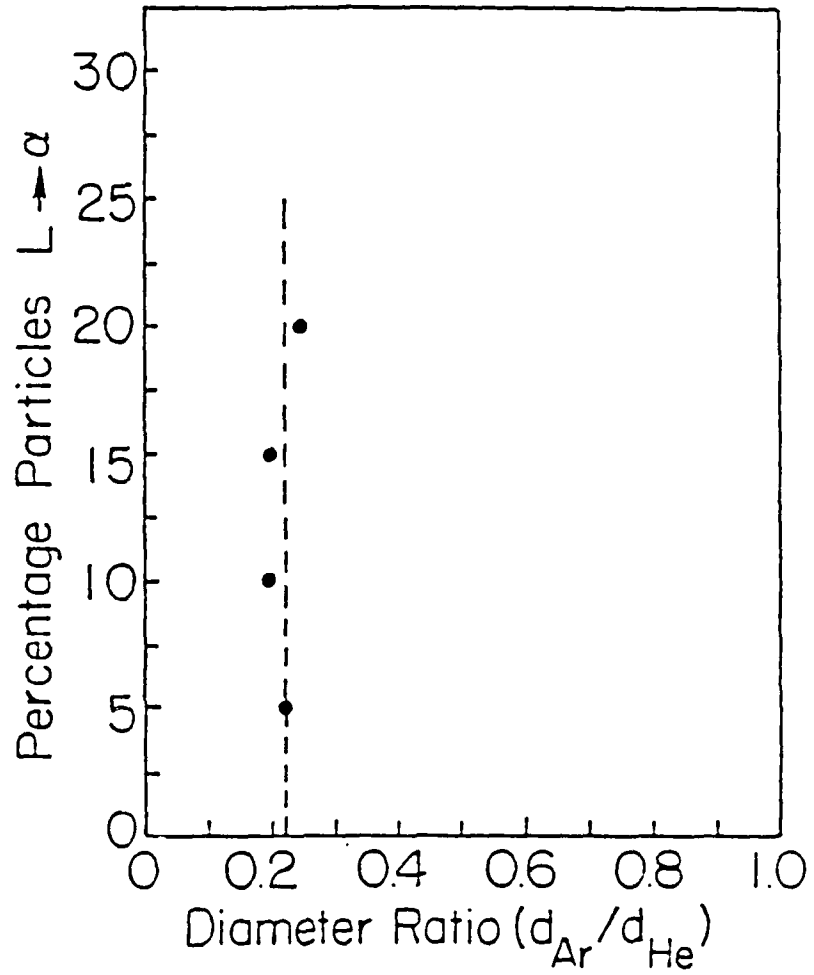


Figure 29. Summary of the diameter ratio for Ar and He drop tube processed powder as a function of metastable product structure abundance in Ti-40 at. % Al.

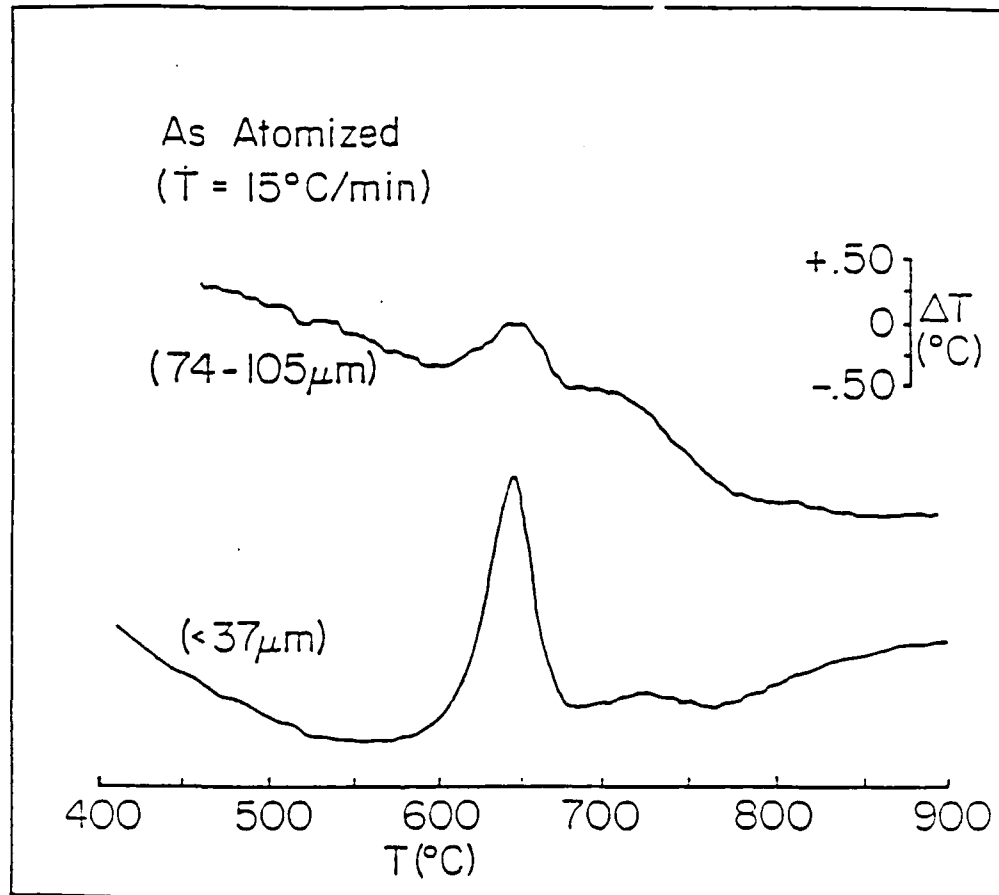


Figure 30. DTA results for continuous heating of fine and coarse atomized Ti-48 at. % Al powder.

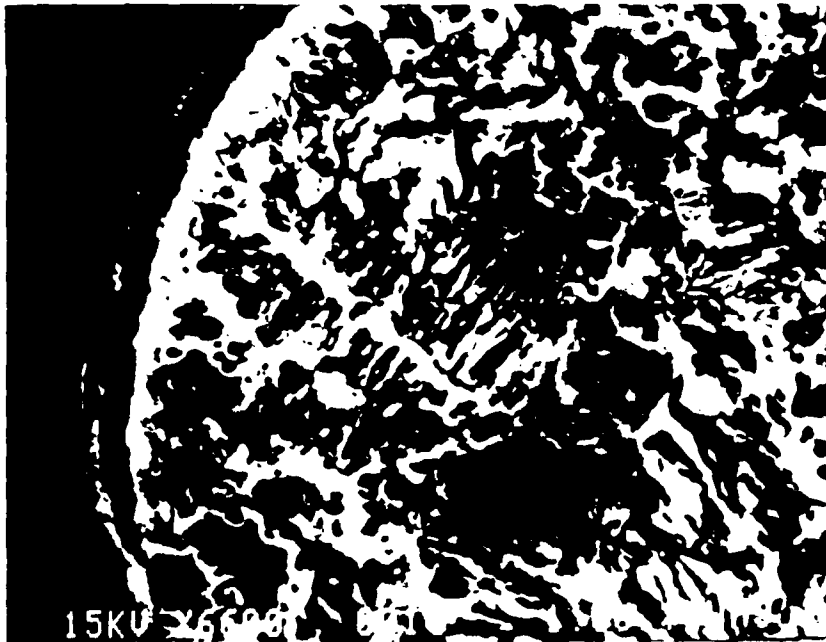
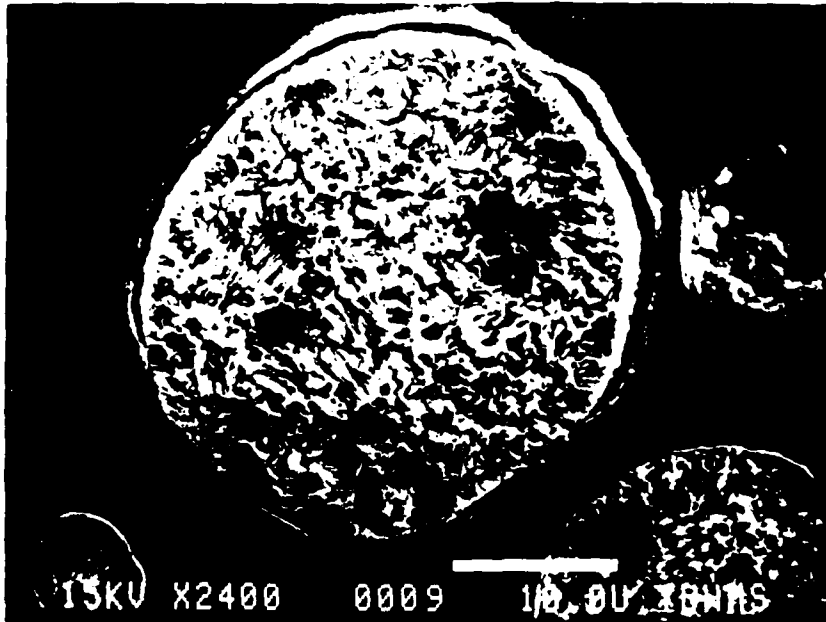


Figure 31. SEM micrographs showing decomposed microstructure of atomized Ti-48 at. % Al powder following an anneal of 900°C.

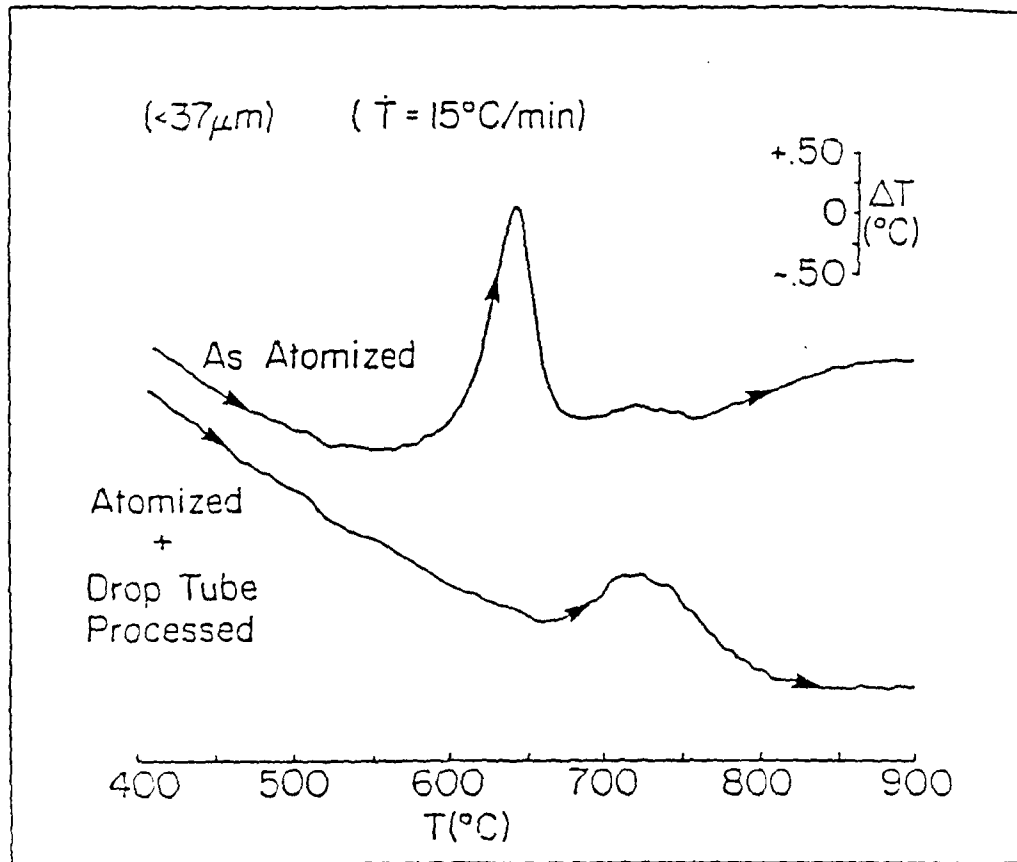


Figure 32. Comparison of decomposition behavior for atomized and drop tube processed (He) Ti-48 at. % Al.

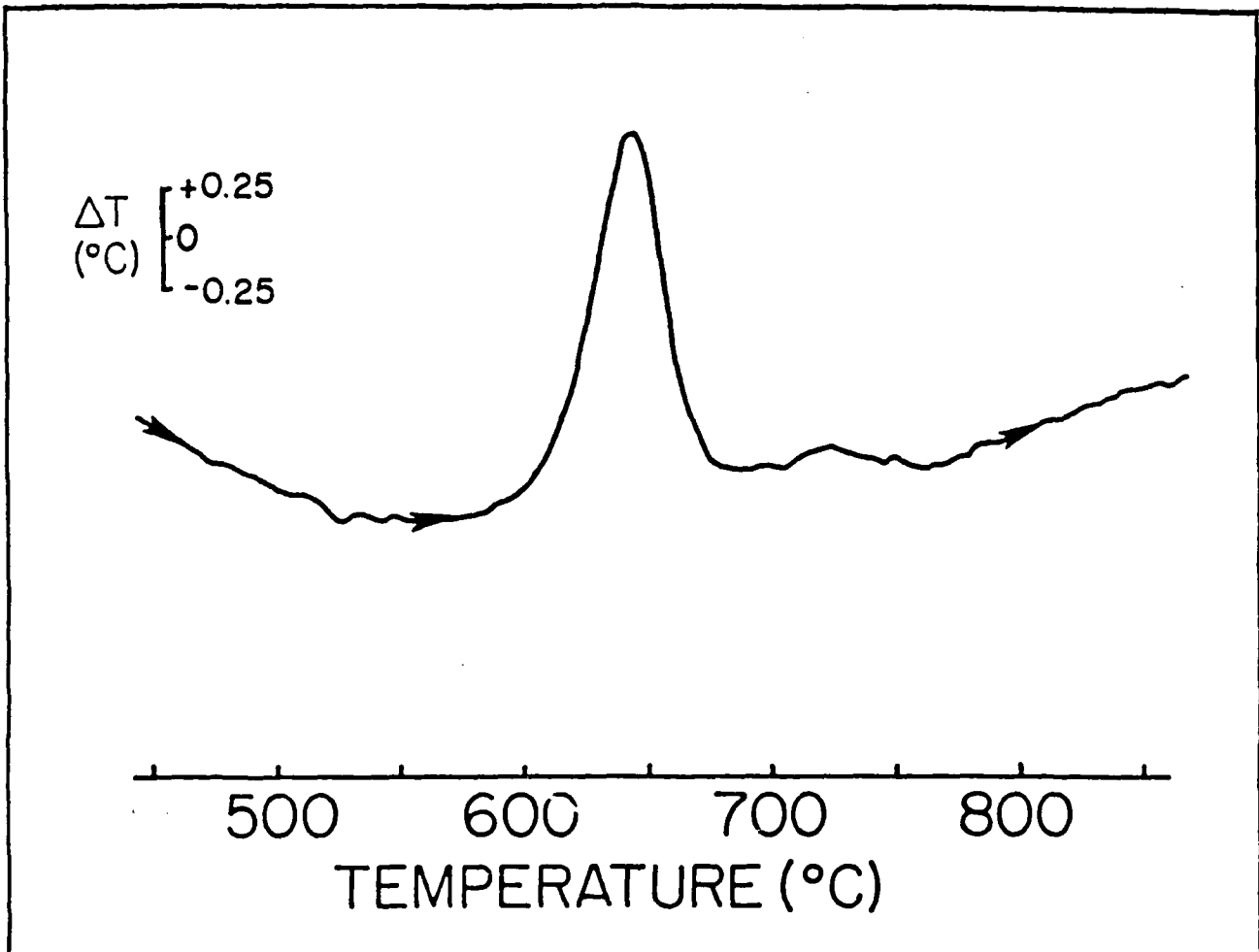


Figure 33. Differential thermal analysis (DTA) trace showing decomposition exotherm upon initial heating of the metastable α_2 ($<44\mu\text{m}$) powder of equiatomic composition.

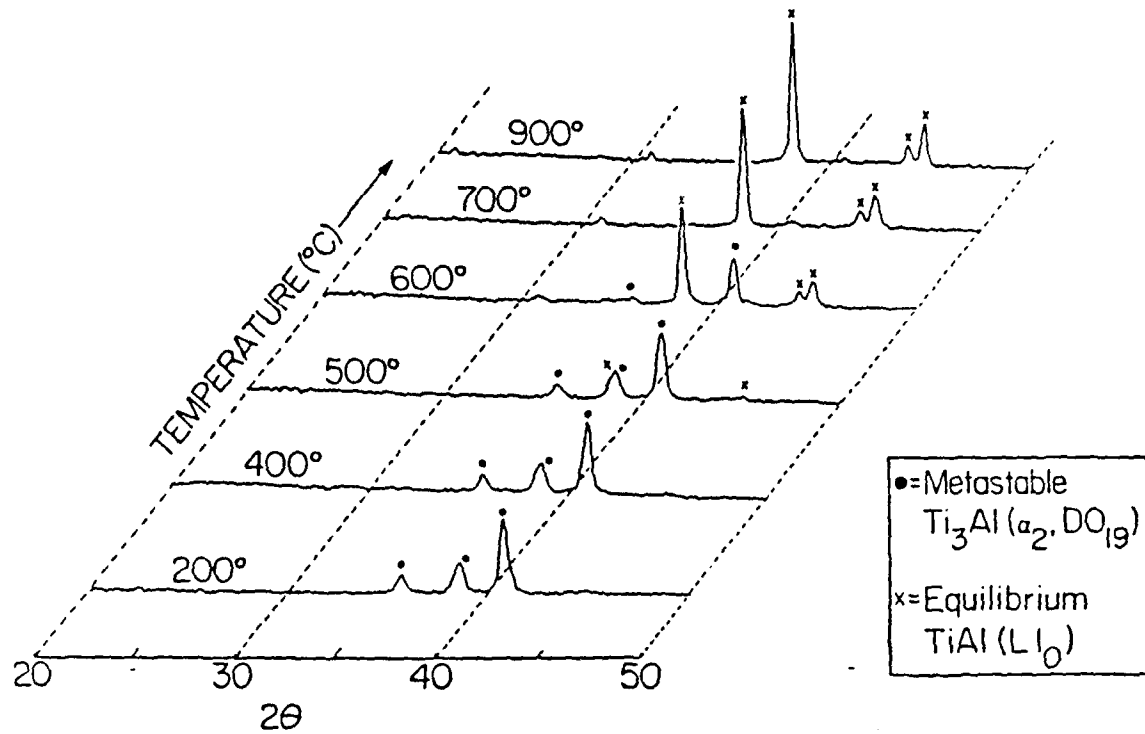


Figure 34. Summary of x-ray diffraction patterns showing decomposition of metastable α_2 to equilibrium TiAl in $<44\mu\text{m}$ powder of Ti-50 at. % Al during step scan annealing treatments.

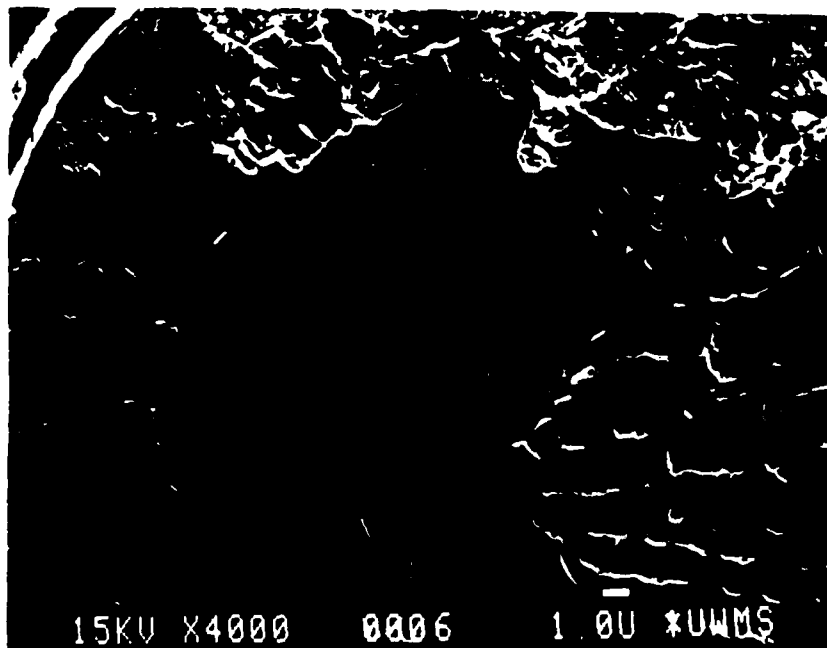
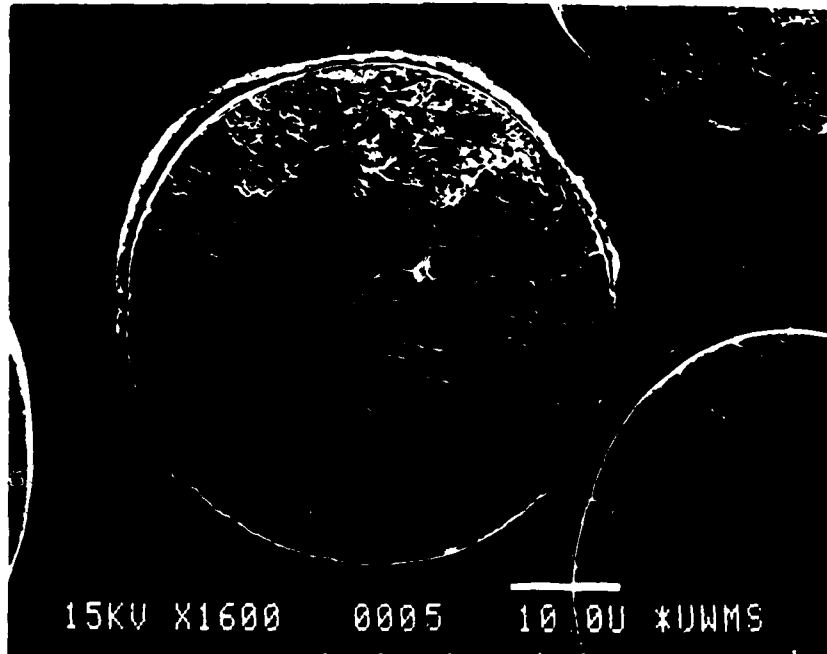


Figure 35. SEM micrographs showing development of a plate morphology during decomposition of α_2 to TiAl in Ti-50 at. % Al powder annealed at 600°C for one hour.



Figure 36. TEM micrographs showing alternating plates of α_2 and TiAl formed during partial decomposition of melt spun Ti-56 at. % Al ribbon.

Nb-Ti-Al 1200 °C

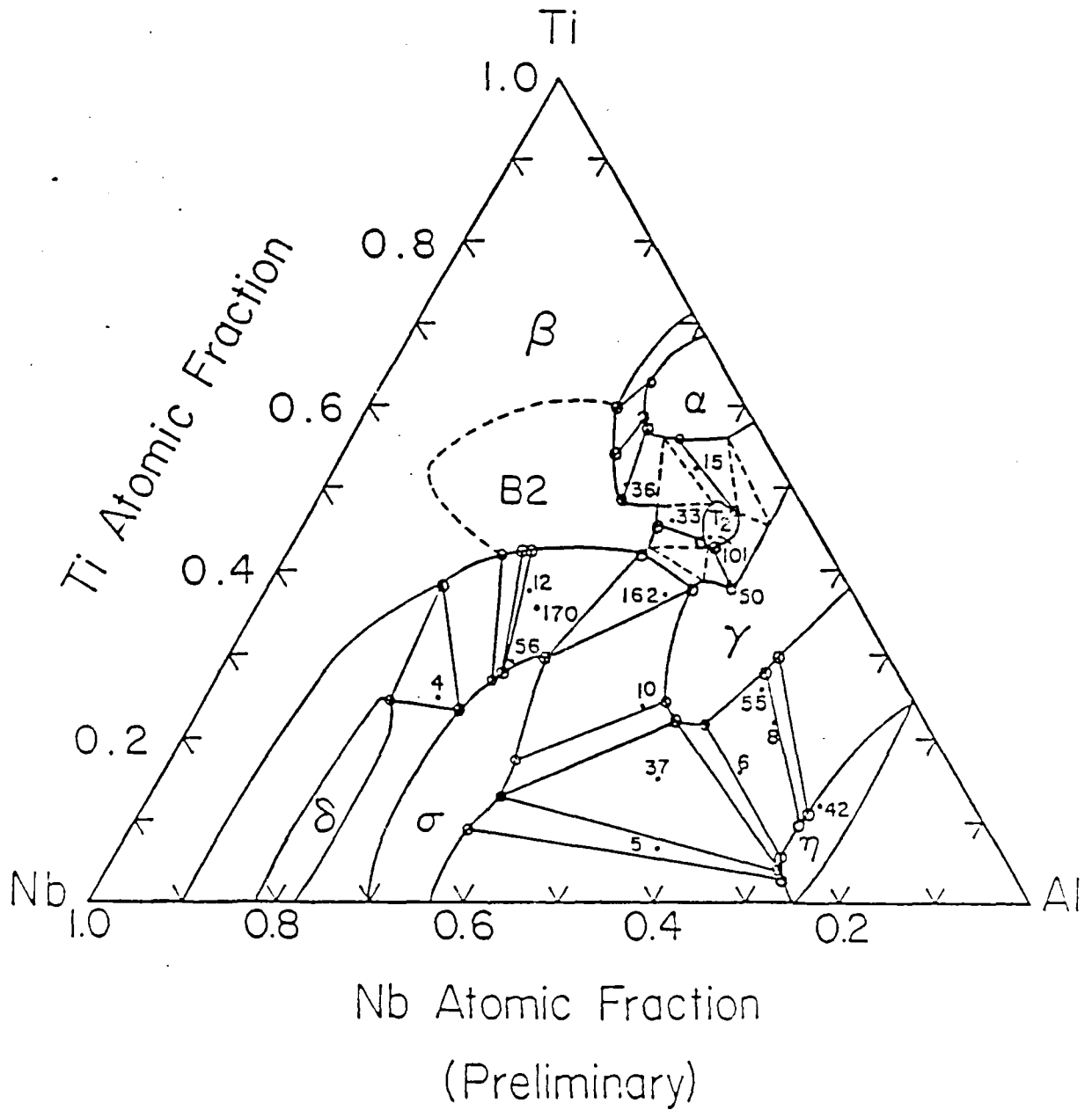


Figure 37. Isothermal section at 1200°C in the Nb-Ti-Al ternary system. Note the B2 single phase field in center of the phase diagram.

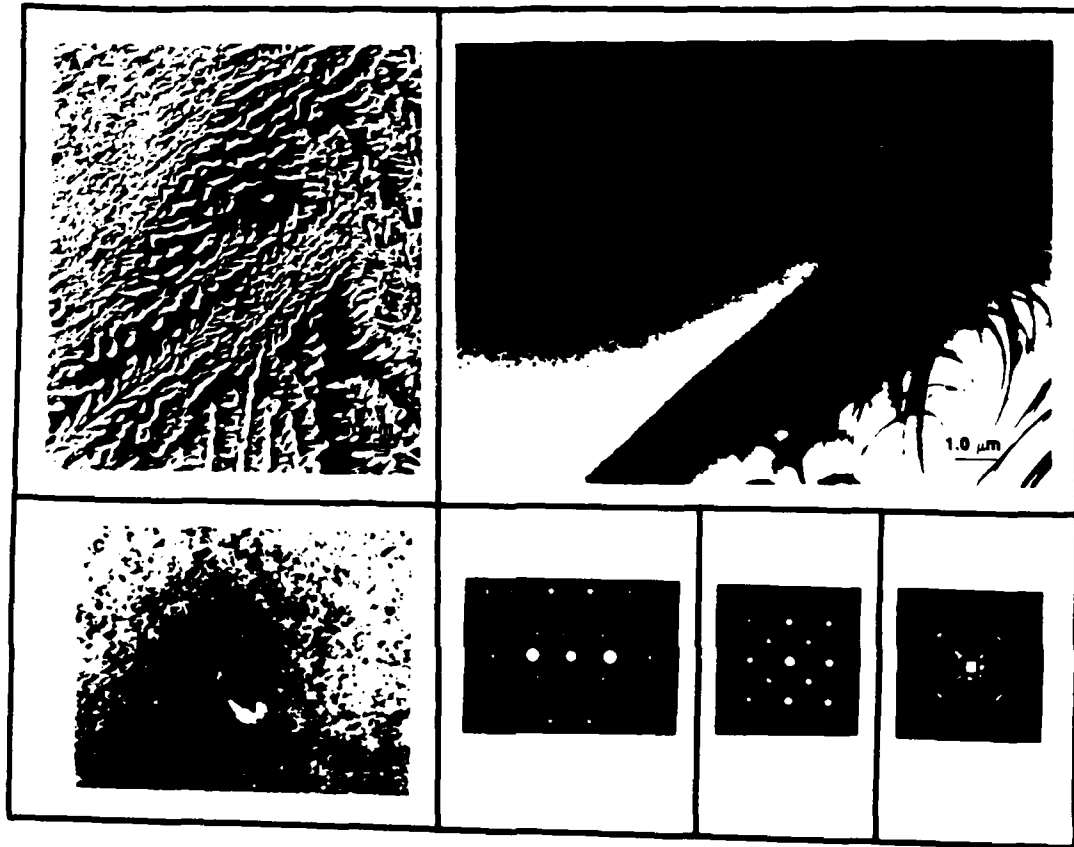


Figure 38. Alloy 36 annealed at 1200°C for 14 days: a) optical micrograph; b) TEM micrograph; c) enlargement of precipitate-bearing grain in b); d) SAD pattern spots; e) [110] B2 zone with superimposed B8₂ illustrating 4m symmetry.

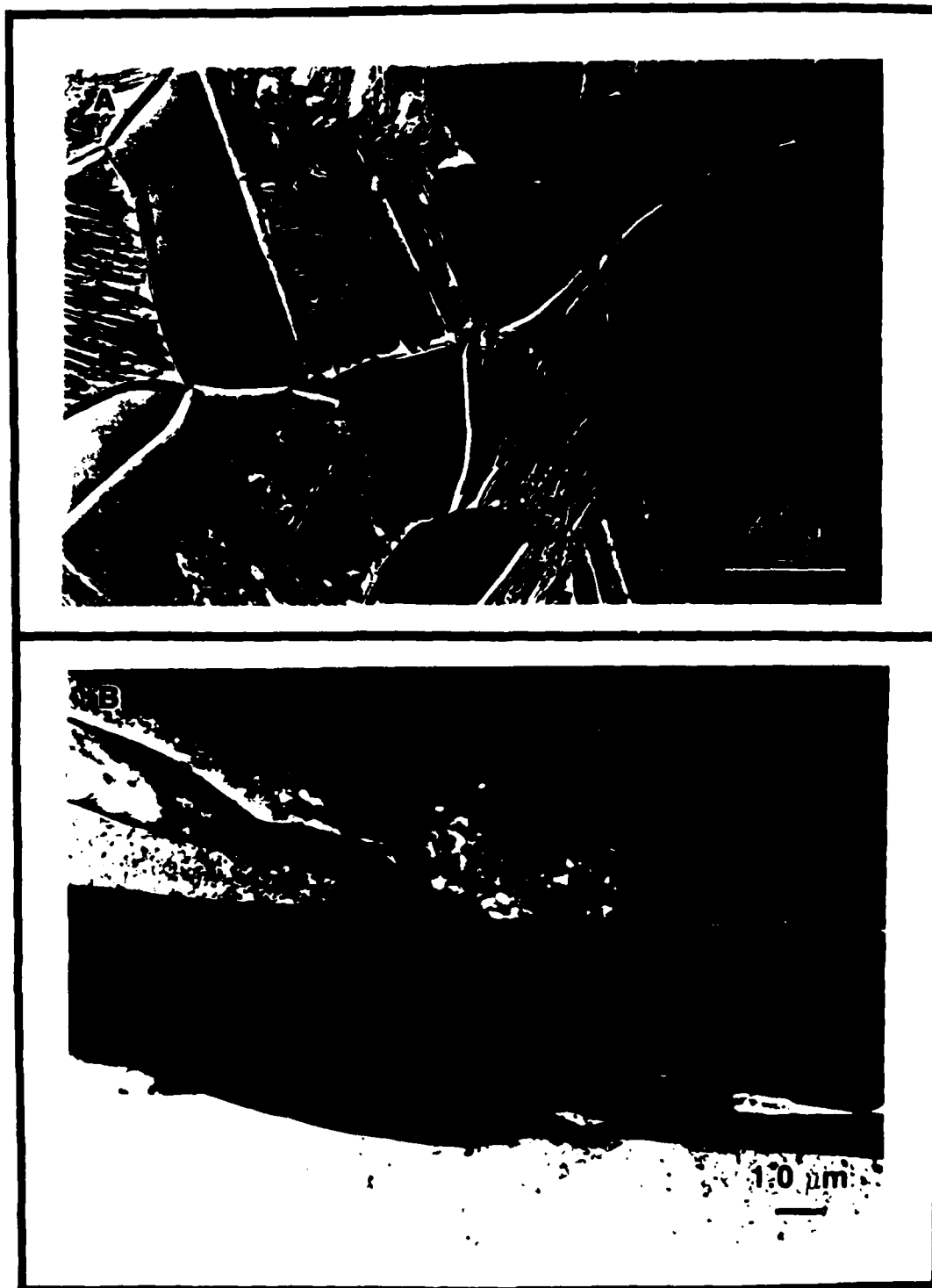


Figure 39. a) Photomicrograph of $Nb_{10}Ti_{53}Al_{37}$ after annealing at $1200^{\circ}C$ for 14 days;
b) TEM micrograph of non-smooth grains in a).

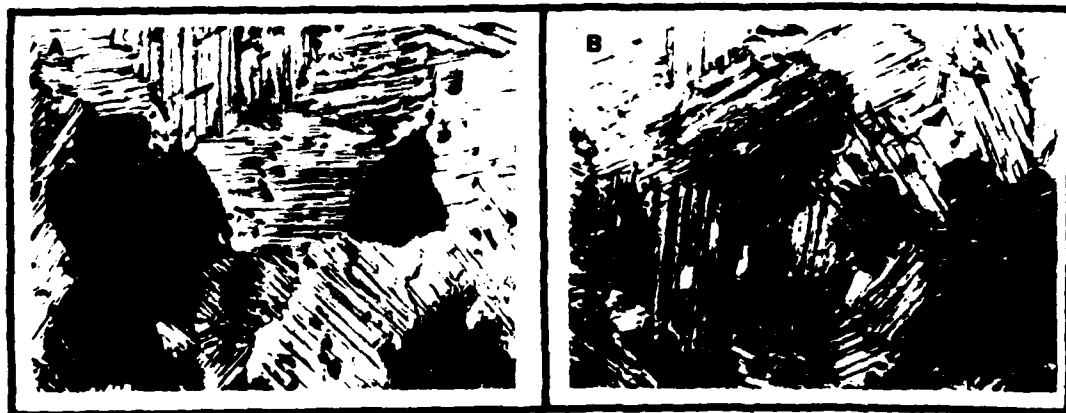


Figure 40. Photomicroscopy of $\text{Nb}_{11}\text{Ti}_{45}\text{Al}_{44}$ annealed at 1200°C and followed by a) slow cooling and b) quenching.



Figure 41. a) TEM micrograph of $\text{Nb}_{11}\text{Ti}_{45}\text{Al}_{44}$ after quenching from 1200°C , regions a) through g) are B2 phase; b) SAD pattern; c) CBED pattern of $[100]$ B2 zone; d) SAD pattern; e) CBED pattern of $[111]$ B2 zone.

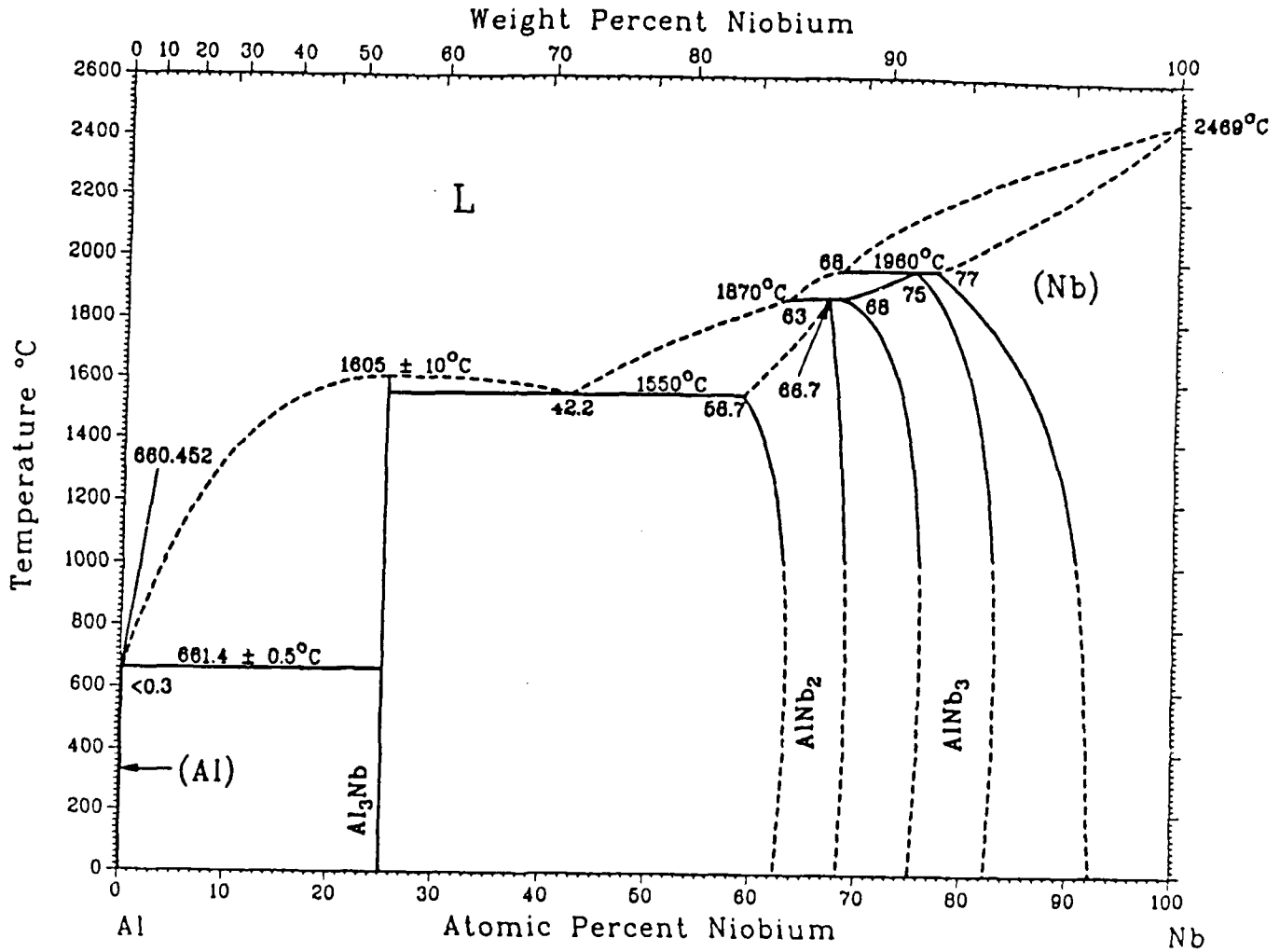


Figure 42. Nb-Al equilibrium phase diagram.

Al - 66.7 at. %Nb: X-RAY RESULTS

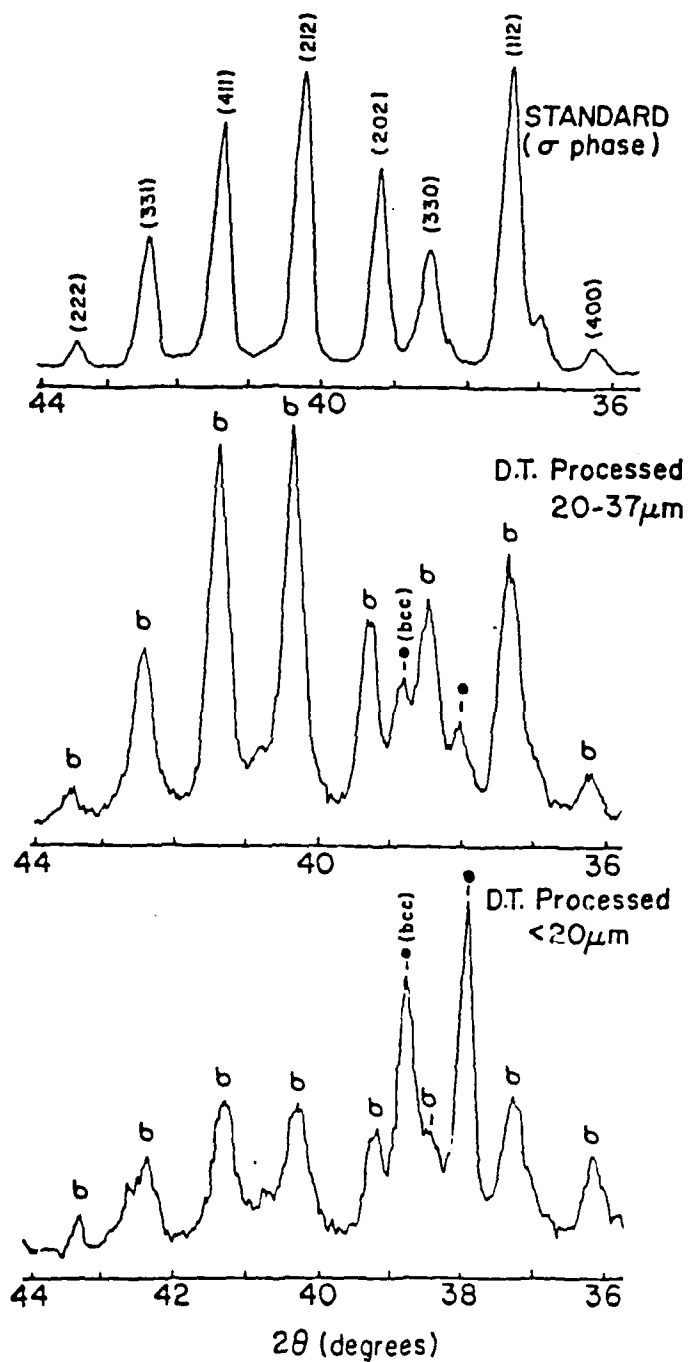


Figure 43. Summary of x-ray diffraction results for Nb-33 at. % alloy powder of equilibrium σ phase and drop tube processed powder samples.

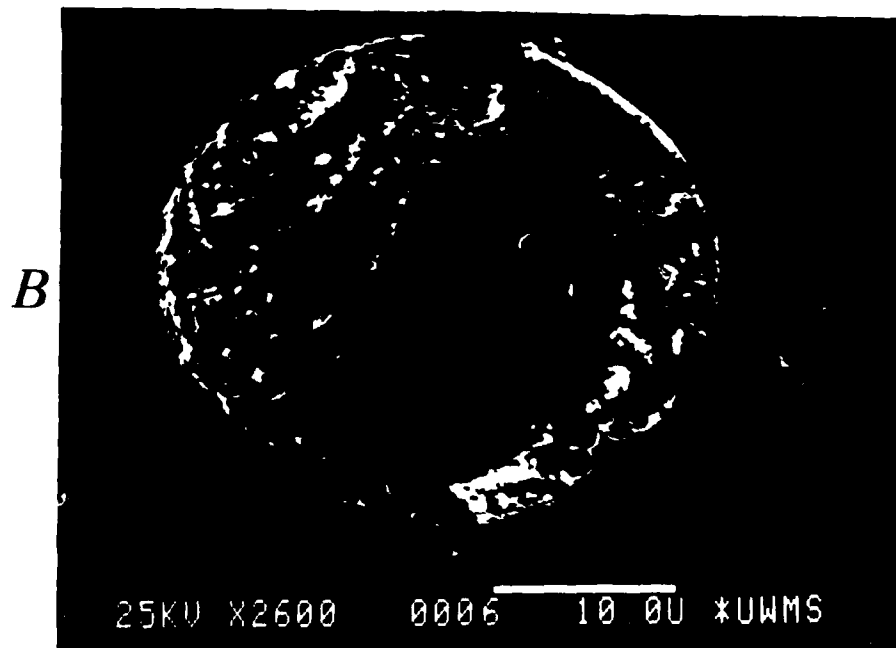
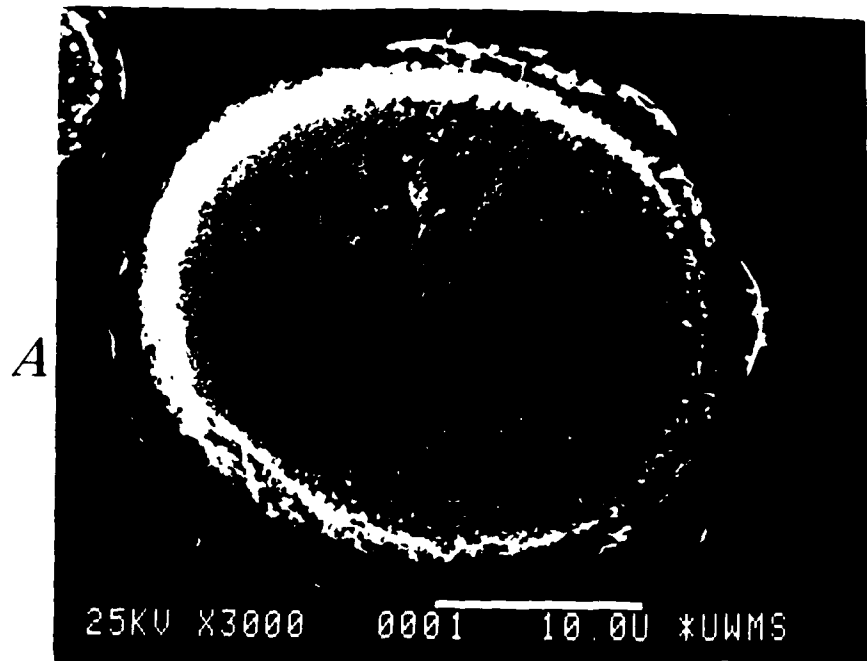


Figure 44. SEM micrographs of Nb-33 at. % Al showing microstructures developed in $<20\mu\text{M}$ powder with a) typical of fine powder and b) most often observed in larger powder.

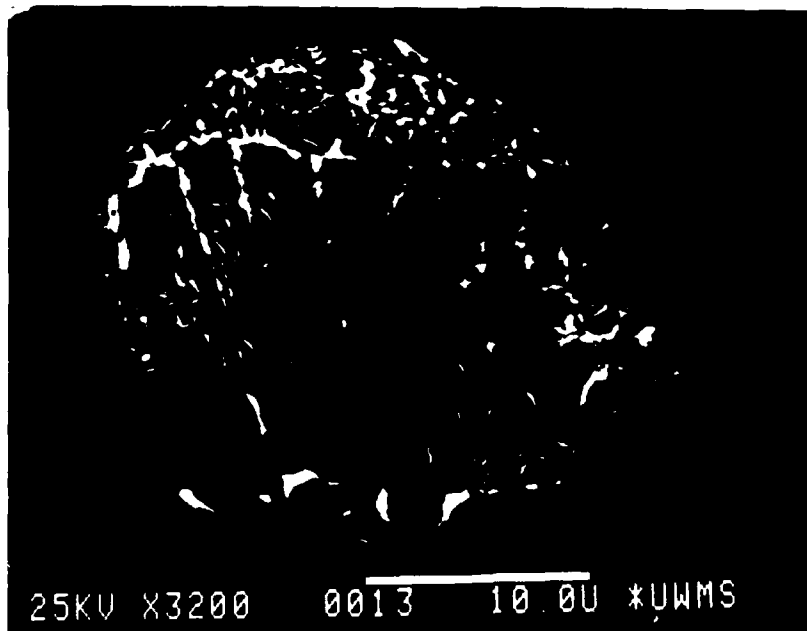


Figure 45. SEM micrographs of Nb-33 at. % Al showing microstructural development in 20-37 μm powder following drop tube processing.

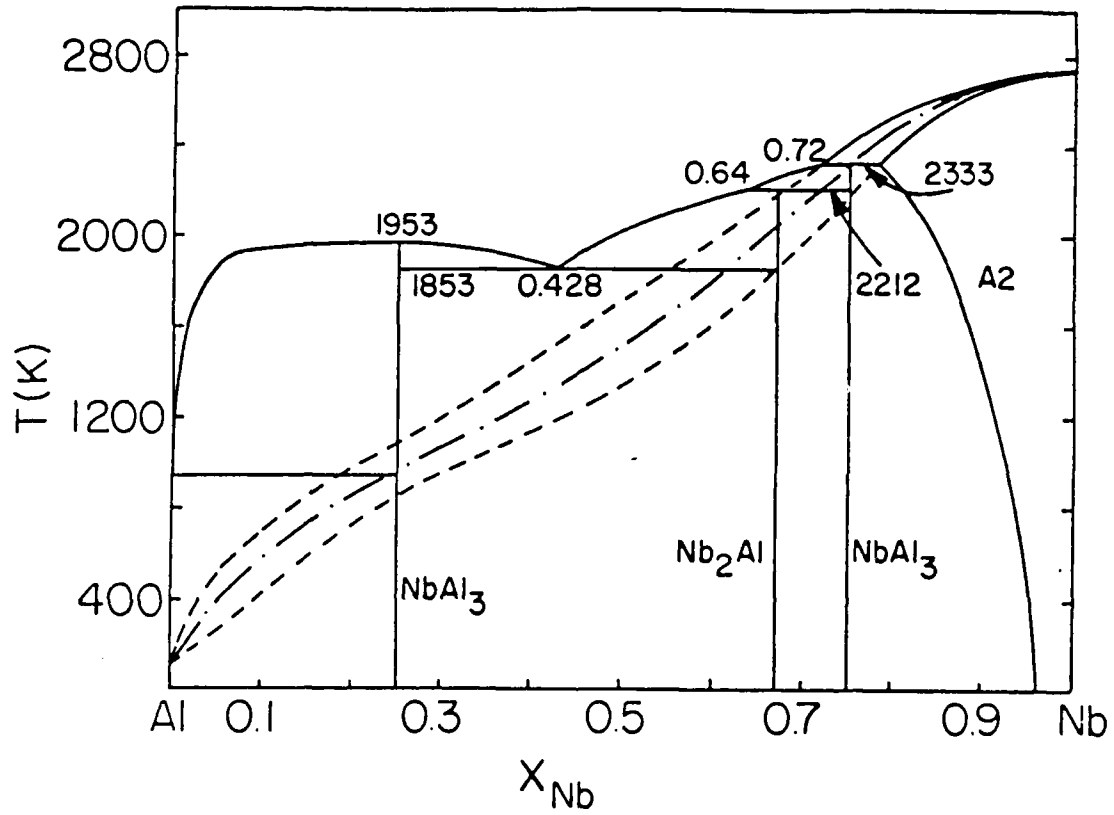


Figure 46. Nb-Al phase diagram showing metastable extension of Nb solid solution phase field.

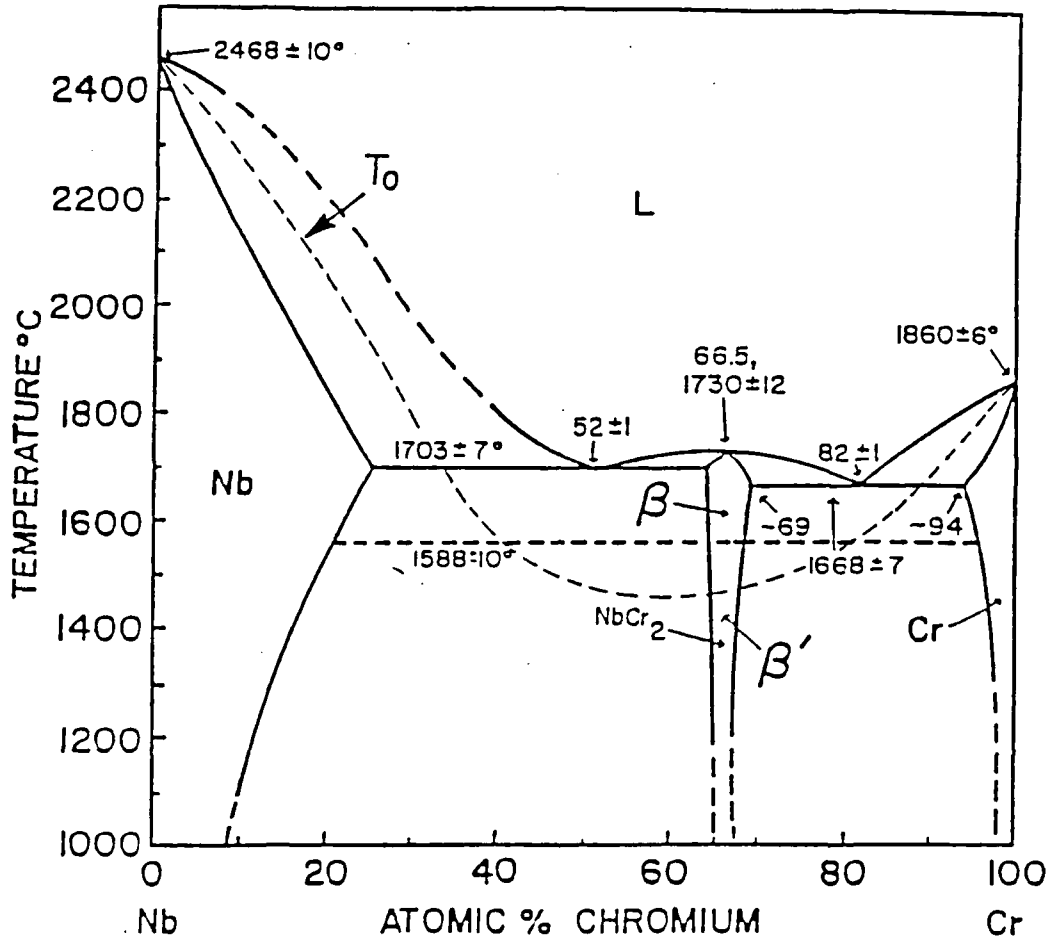


Figure 47. Nb-Cr phase diagram.

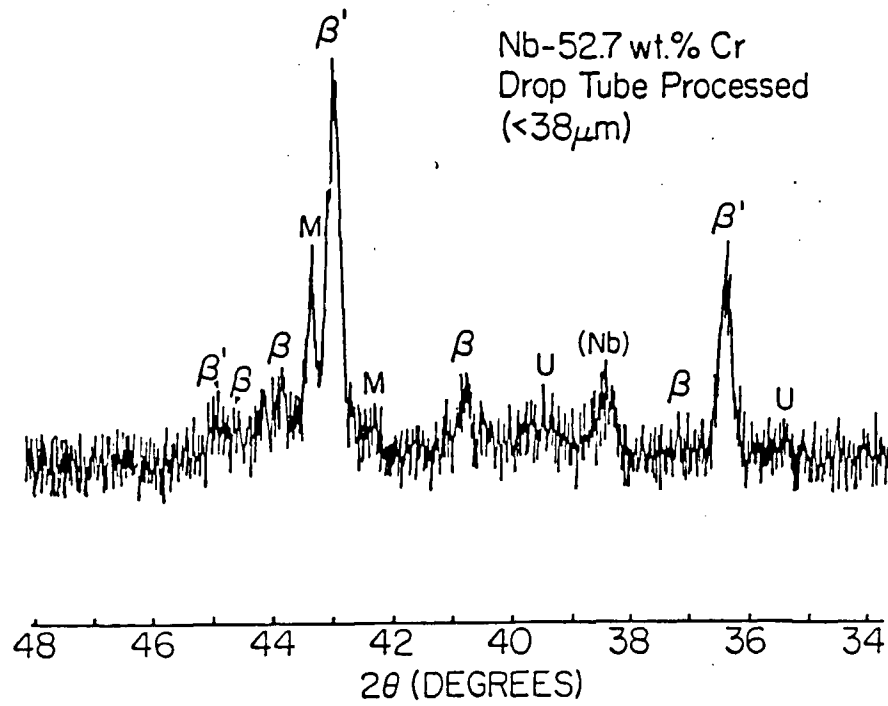


Figure 48. X-ray diffraction scan of fine Nb-52.7 wt. % Cr powder after drop tube processing. Diffraction peaks labeled "M" and "U" refer to unknown phases.

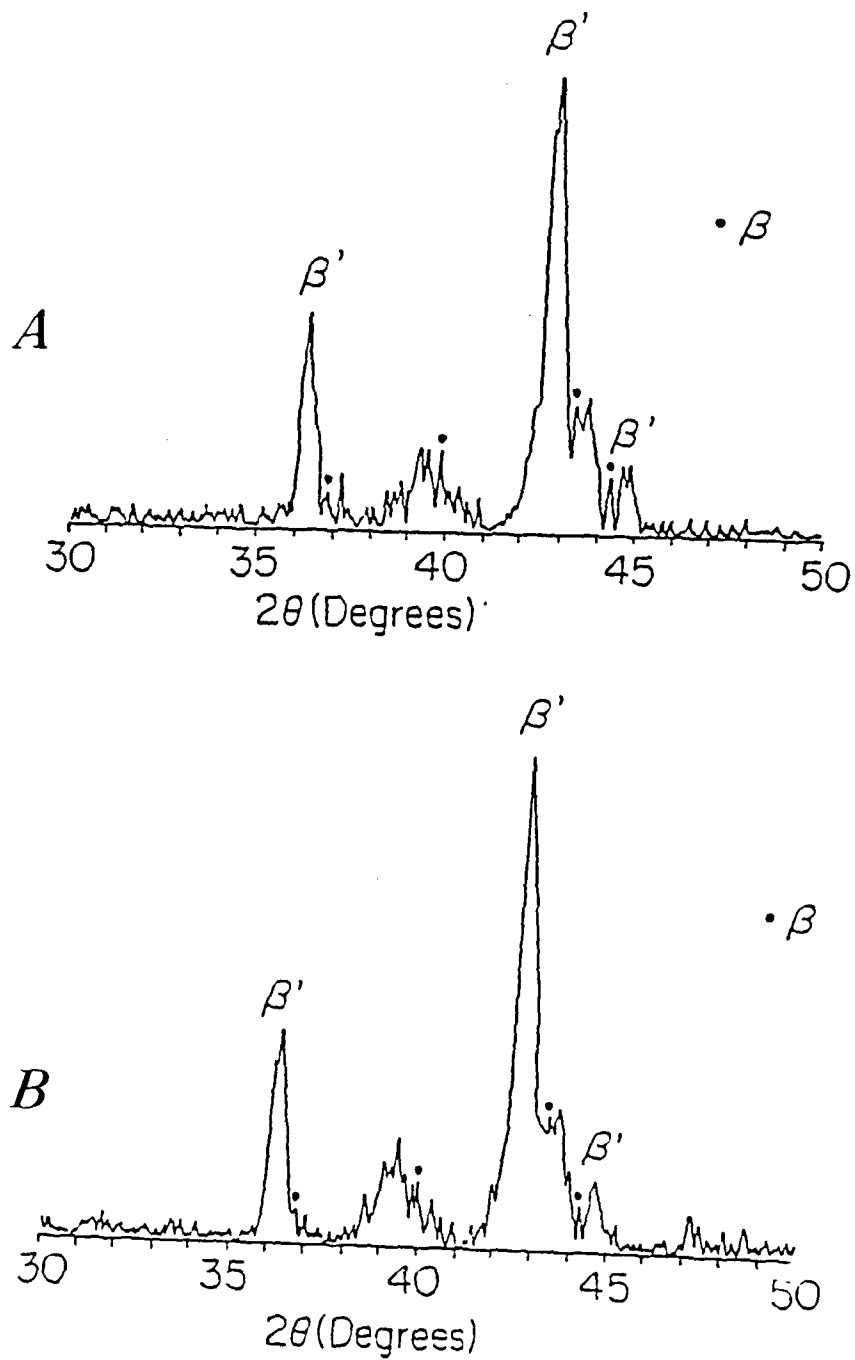


Figure 49. a) X-ray diffraction scan of splat quenched NbCr_2 ; b) splat quenched NbCr_2 heat treated for one hour at 600°C .

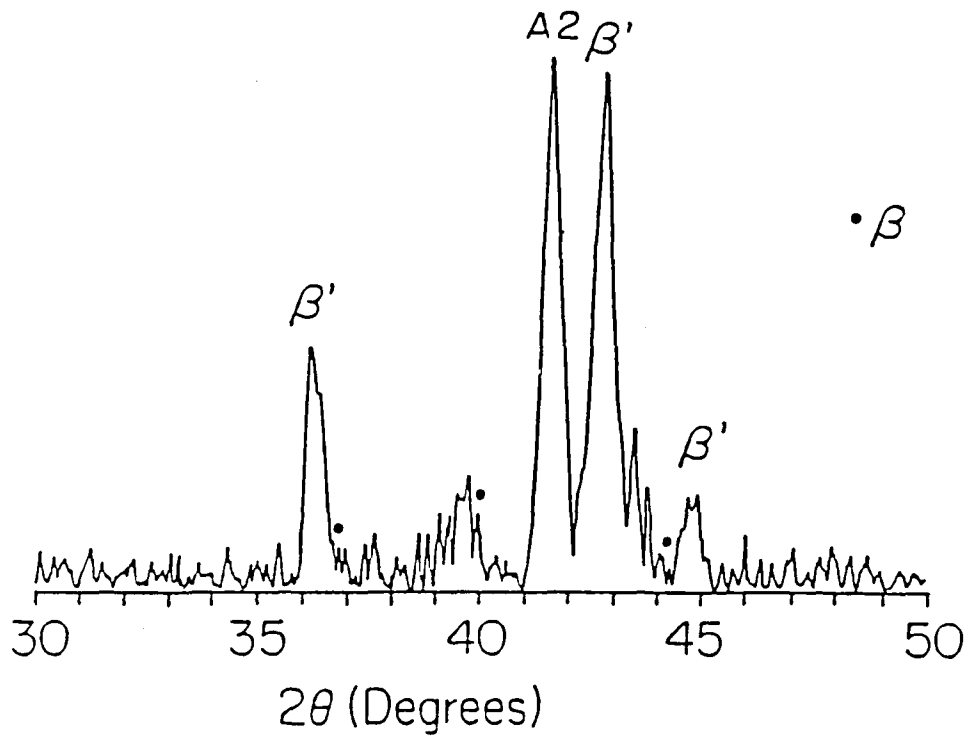


Figure 50. X-ray diffraction scan for splat quenched $\text{NbCr}_2 + 10 \text{ wt. } \% \text{ Ti}$.

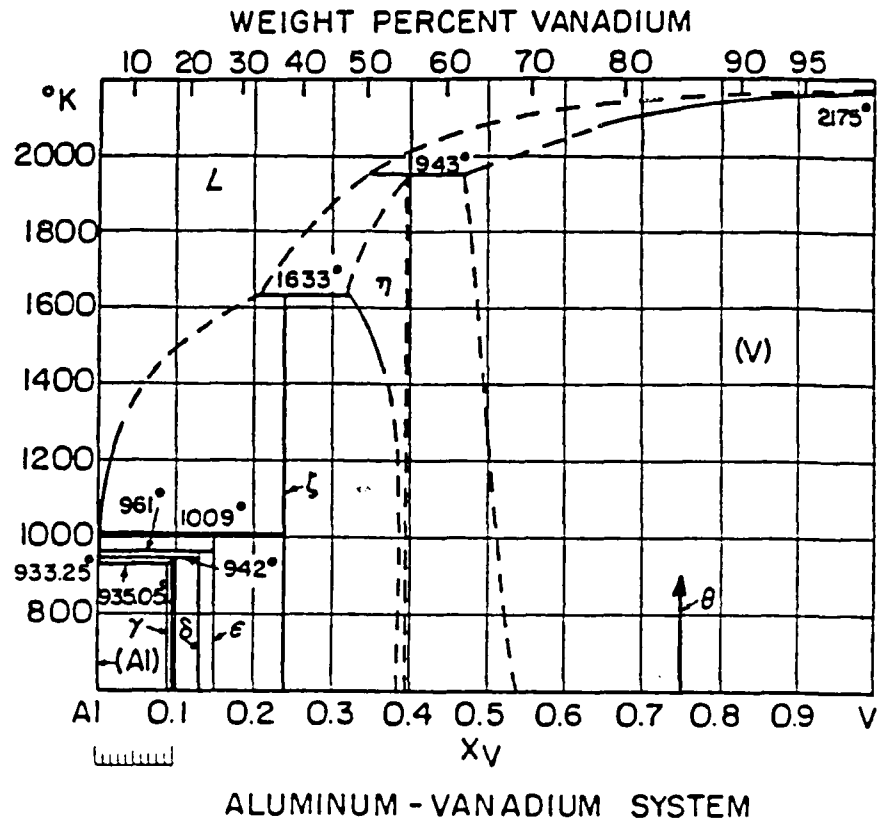


Figure 51. Al-V phase diagram.

VII. References

1. J. L. Murray, in "Phase Diagrams of Binary Titanium Alloys" ed. J. L. Murray (ASM, Metals Park, OH) 12 (1987).
2. A. J. Goldak and J. G. Parr, Trans. AIME 221, 639 (1961).
3. F. H. Fores and D. Eylon, Powder Met. Int. 17, 235 (1985).
4. W. W. Liang, Y. A. Chang, S. Lau and I. Gyuk, Acta Met. 21, 629 (1973).
5. T. W. Clyne, R. A. Ricks and P. J. Goodhew, Intl. J. Rapid Solid. 1, 59 (1985).
6. C. Troiana and Tokich, Trans. AIME 175, 728 (1948).
7. T. E. O'Connell and P. A. Flinn, "Titanium and Titanium Alloys", eds. J. C. Williams and A. F. Belov (Plenum Press, NY) 1451 (1982).
8. M. J. Blackburn, "The Science, Technology and Application of Titanium", R. Jaffee and N. Promisel, eds., (Pergamon Press, Edinburgh, U.K.) 633 (1970).
9. J. K. Tien, P. G. Shewmon and J. S. Foster, Met. Trans. 2 1193 (1971).
10. T. K. G. Namboodhiri, G. J. McMahon Jr. and H. Herman, Met. Trans. 4, 1323 (1973).
11. S. M. L. Satry and H. A. Lipsitt, Met. Trans. 8A, 1543 (1977).
12. T. E. O'Connell and P. A. Flinn in, *Titanium and Titanium Alloys*, J. C. Williams & A. F. Belov eds., (Plenum Press, NY.) 1451 (1982).
13. H. A. Lipsitt, Mat. Res. Soc. Symp. Proc., 351 (1985).
14. R. Strychor, J. C. Williams and W. A. Soffa, Met. Trans. 19A, 1321 (1988).
15. D. Banerjee, A. K. Gogia, T. K. Naudi and V. A. Joshi, Acta Met. 36, 871 (1988).
16. S. M. L. Sastry and H. A. Lipsitt, Met. Trans. 8A, 1543 (1977).
17. K. Muraleedharan and D. Banerjee, Met. Trans. 20A, 1139 (1989).
18. L. A. Bendersky and W. J. Boettinger, Mat. Res. Soc. Symp. Proc. 133, 45 (1989).

19. D. G. Konitzer, I. P. Jones and H. L. Fraser, Scripta Met. 20, 265 (1987).
20. D. Banerjee, T. Naudi and A. K. Gogia, Scripta Met. 21, 597 (1987).

VIII. Publications of the Current Program

During a research program substantial time intervals often elapse between the completion of a research study, submission of a manuscript and the final appearance of a paper in print. As a result, the following list gives publications in preparation as well as those in print or in press.

- 1) "Microstructural Development in Rapidly Solidified TiAl", J. A. Graves, J. H. Perepezko, C. H. Ward and F. H. Fores, *Scripta Met.* 21, 567 (1987)
- 2) "RSP Pathways for Alloy Design", J. H. Perepezko, B. A. Mueller, and J. A. Graves, in *Rapid Solidification Processing: Principles and Technology IV*, R. Mehrabian and P. A. Parrish eds., (Claitors Pub. Div., Baton Rouge, La) pg. 99 (1988)
- 3) "Pathway for Microstructural Development in TiAl", L. A. Bendersky, J. A. Graves, F. S. Biancaniello, J. H. Perepezko and W. J. Boettinger, *Mat. Sci. Eng.* 98, 265 (1988)
- 4) "Phase Selection in Undercooled Liquids of Pulsed-Laser Melted Alloys", D. M. Follstaedt, P. S. Peercy and J. H. Perepezko, *Mat. Res. Soc. Symp. Proc.* 100, 573 (1989)
- 5) "Microstructural Development in Ti-Al Alloys During Rapid Solidification", J. C. Mishurda, J. H. Perepezko, J. A. Graves and F. H. Fores, in *Sixth World Conference on Titanium* J. Berger ed. (Jouve, Paris) p. 1127 (1989)
- 6) "Processing of Undercooling Melts", J. H. Perepezko and W. P. Allen, in *Third International Colloquium on Drops and Bubbles*, T. Wang ed. (American Inst. of Physics, NY) 197, 289 (1989)
- 7) "High Temperature Phase Stability in the Ti-Al-Nb System", J. H. Perepezko, Y. A. Chang, L. E. Seitzman, J. C. Lin, N. R. Bonda, T. J. Jewett and J. C. Mishurda in *High Temperature Aluminides & Intermetallics*, S. H. Whang, C. T. Liu, D. P. Pope and J. O. Stiegler eds., (TMS, Warrendale PA) pg. 19 (1990)
- 10) "Decomposition of an Ordered BCC Phase in $Ti_{45}Al_{44}Nb_{11}$ ", L. E. Seitzman and J. H. Perepezko (in preparation)
- 11) "Solidification Processing of NbCr₂ Alloys", D. J. Thoma and J. H. Perepezko, *Mat. Res. Soc. Symp. Proc.* (in press)
- 12) "Decomposition Reactions and Toughening in NiAl-Cu Alloys", W. P. Allen, J. C. Foley, R. F. Cooper and J. H. Perepezko, *Mat. Res. Soc. Symp. Proc.* (in press)

IX. Presentations

- 1) "RSP Pathways for Alloy Design" Rapid Solidification Processing: Principles and Technologies IV, Santa Barbara, CA (1987)
- 2) "Phase Selection in Undercooled Liquids of Pulsed-Laser Melted Alloys", Materials Research Society Symposium, Boston, MA (1987)
- 3) "Microstructure Evolution During Rapid Solidification", DARPA Workshop on Mathematical Modeling of Materials Processing, Greenbriar, W. VA (1988)
- 4) "Processing of Undercooling Melts", Third Internat. Colloquium on Drops and Bubbles, Monterey CA (1988)
- 5) "Microstructural Development in Ti-Al Alloys During Rapid Solidification", Sixth World Conference on Titanium, France (1988)
- 6) "Solidification of High Temperature Intermetallic Alloys" DARPA Materials Research Council, La Jolla CA (1988)
- 7) "Solidification Processing of Ti-Al Alloys", Annual Meeting of Light Metals Center, University of Virginia (1989)
- 8) "High Temperature Phase Stability in the Ti-Al-Nb System", TMS-AIME Fall Meeting (1989)
- 9) "Decomposition Reactions and Toughening in NiAl-Cu Alloys", Materials Research Society Symposium, San Francisco CA (1990)
- 10) "Solidification Processing of NbCr₂ Alloys", Materials Research Society Symposium, San Francisco CA (1990)
- 11) "Solidification Processing of Intermetallics", Naval Research Laboratory, Washington DC (1990)

X. Participating Scientific Personnel

- 1) Professor J. H. Perepezko, Principal Investigator
- 2) Dr. L. E. Seitzman, Postdoctoral Fellow
- 3) Dr. N. R. Bonda, Postdoctoral Fellow (half time)
- 4) J. A. Graves, Graduate Student, PhD in 1987
- 5) J. C. Mishurda, Graduate Student, MS in 1987, currently working on PhD
- 6) D. J. Thoma, working on PhD
- 7) W. P. Allen, working on PhD (to be completed October 1990)
- 8) P. S. Frankwicz, working on PhD